Supplementary Information (SI) for Energy & Environmental Science.

Supporting Information

Anti-dissolving Fe_2N_6 Sites Based Carbon Fiber Membranes for Binder-free Zn-air Batteries with a 200-Day Lifespan

Zian Xu **et. al.**

1. Experimental Section

1.1 Chemicals

1,4,5,8-naphtalene tetracarboxylic acid (NTCA, 98%, Zhengzhou Alfa Chemical Co.), poly(vinyl pyrrolidone) (PVP, Mw: 360,000, Meryer Chemical Co.), 1,3,5-tris(4-aminophenyl)benzene (TAPB), iron(III) acetylacetonate (99%, Shanghai Bodi Biotechnology Co., Ltd.) and N,N-dimethylformamide (DMF, 99.9%, Aladdin Bio-Chem Technology Co.) were used without further purification.

1.2 Synthesis of Fe_2N_6-CMPCFs and other contrast samples

In a typical procedure, 0.456 g (1.5 mmol) NTCA, 0.351 g (1 mmol) TAPB and 90 mg PVP were mixed and dissolved in 2.7 mL DMF. The total concentration of the mixed solution was 25 wt.%. After stirring for 10 h at room temperature, 27 mg of the iron (III) acetylacetonate (3 wt.% content of the solid) was added, followed by stirring for 1 h to get the precursor solution for electrospinning.

During the electrospinning process, the applied voltage was controlled at 14 kV and the feed rate of the mixture solution was 0.7 mL h^{-1}. A rotated roller covered with an aluminous foil with the distance of 20 cm to the needle was adopted as the collector. The obtained nanofiber membranes were heat-treated under Ar atmosphere with the following step-by-step procedure to promote the polycondensation of monomers: 1) heat treatment at 150 ℃ for 60 min; 2) increasing the temperature to 300 ℃ and annealing for another 60 min; 3) further heat treatment at 420 ℃ for 60 min for the complete reaction between the monomers and removal of the PVP to obtain the CMP fiber membranes. The reaction equation of the two monomers is shown in Figure S1. The carbonization of the CMP membrane was carried out at the temperature of 900 ℃ for 60 min. Later, the temperature of the furnace was decreased to 800 ℃ and started the importation of NH_3 for annealing for the last 30 min. The volume ratio of Ar and NH_3 was controlled on 5:1. The heat rates of the whole procedure were controlled at 5 ℃ min^{-1}. The obtained carbon nanofiber membrane was named as Fe_2N_6-CMPCFs.

The samples were prepared using other iron (III) acetylacetonate contents of 1 wt.%

and 5 wt.% following the same procedure as Fe_2N_6-CMPCFs, which were named as FeN_4-CMPCFs and Fe NPs-CMPCFs, respectively. The contrast samples without Fe dopant and without NH_3 were prepared and named as CMPCFs and Fe-CMPCFs-Ar, respectively. At last, the prepared carbon membranes were immersed into a 3.0 M H_2SO_4 solution at 80 °C for 6 h. After rinsing, the samples were heated again at 900 °C for 1 h in the Ar atmosphere.

1.3 Sample Characterization

Powder X-ray diffraction patterns were recorded on Rigaku D8, with a Cu K αradiation (λ= 0.15406 nm), to investigate the crystal structure. The morphology of as-prepared catalysts was observed with scanning electron microscopy (SEM, TESCAN MIRA3). Scanning transmission electron microscopy (STEM) (ScientificTM Talos F200X) and high angle annular dark-field scanning (HAADF-STEM) with a spherical aberration corrector (Titan Themis G2) were performed to detect the structure of as-prepared samples at the atomic level. The elemental distribution was obtained by the corresponding energy dispersive spectroscopy of HAADF-STEM. The surface composition for as-prepared samples were tested by X-ray photoelectron spectroscopy (XPS, Escalab Xi^+) with monochromatic Al Kα (1486.6 eV) radiation. Raman spectroscope was adopted on HORIBA LabRAM HR Evolution, to reflect structural defect of catalysts, where the Ar^+ laser with 514 nm wavelength is used as the source of radiation. The specific surface areas were measured by isothermal N_2 adsorption/desorption isotherms (Micromeritics, ASAP2460-4, SIN 420) and the pore size distribution was analyzed by BJH and BET model. Fourier transform infrared spectra (FTIR, PerkinElmer) and solid-state 13C nuclear magnetic resonance spectroscopy (NMR, Bruker AVANCE III HD 600WB) were adopted to verify the structure of polymerized CMP. Thermogravimetric analysis (TGA 55, TA Instruments, USA) was used to estimate the carbon yield of final products. X-ray absorption fine structure (XAFS) was detected at the 1W1B beam line of Beijing Synchrotron Radiation Facility (BSRF). The content of Fe element in all catalysts was characterized by ICP-OES analysis.

1.4 Electrochemical Measurement

The electrochemical ORR tests were performed in O_2-saturated 0.1 M KOH solution by a conventional three electrode system controlled by CHI 760 electrochemical workstation (Shanghai Chenhua Instrument Co., China). The rotating ring-disk electrode (RRDE, Pine Instrument Co, 0.236 cm^{-2}) was employed to load catalysts as a working electrode. And a carbon rod and Hg/HgO electrode were used as the counter and reference electrode, respectively. To prepare the working electrode, 5 mg catalyst was uniformly dispersed in 0.5 mL mixed solution (deionized water: ethanol: 5 wt. % Nafion solution = 19:19:2) with ultrasonication. Then, the catalyst ink was spread on the RRDE surface and dried naturally (loading amount: 0.6 mg cm^{-2}). The commercial 20 wt.% Pt/C (J.M.) sample was used in the same loading content. Cyclic voltammetry (CV) measurements were performed in N_2 or O_2-satureated 0.1 M KOH electrolyte with a scan rate of 50 mV s^{-1} without rotating. Linear sweep voltammetry tests were carried out at 1600 rpm rotating speed with a scan rate of 5 mV s^{-1} with automatic 95% iR compensation. The electron transfer number (n) and H_2O_2 was calculated by the following equation:

$$n = 4 \times \frac{I_d}{I_d + {}^{I_r}\!/_{N}} \tag{1}$$

$$H_2O_2\% = 200 \times \frac{{}^{I_r}\!/_{N}}{I_d + {}^{I_r}\!/_{N}} \tag{2}$$

Where I_d is the measured the disk current and I_r represents the ring current; N is the ring collection efficiency of 0.37. The value of n during ORR was also calculated from the linear slopes of J^{-1} versus $\omega^{-1/2}$ plots based on the Koutecky-Levich (K-L) equation[1]:

$$\frac{1}{J} = \frac{1}{J_K} + \frac{1}{J_L} = \frac{1}{B\omega^{0.5}} + \frac{1}{J_K} \tag{1}$$

$$B = 0.2nFC_0D_0^{2/3}v^{-1/6} \tag{2}$$

$$J_K = nFkC_0 \tag{3}$$

Where J represents the measured current density (mA cm^{-2}); J_k is the kinetic current density (mA cm^{-2}); J_L is the limiting current density (mA cm^{-2}); ω is the angular velocity (rpm); n is the electron transfer number per O_2 molecule; F is the Faraday constant (F= 96,485 C mol^{-1}); D_0 is the O_2 diffusion coefficient in 0.1 M KOH (1.9×10^{-5} cm^2 s^{-1}); v is the kinetic viscosity of 0.1 M KOH (0.01 cm^2 s^{-1}); C_0 stands for the bulk concentration of O_2 (1.2×10^{-3} mol L^{-1}). EIS test was adopted in the frequency ranging from 100 kHz to 0.01 Hz with an amplitude of 5 mV. The accelerated durability test (ADT) to catalysts was conducted with 50 mV/s scan rate from potential 0.4 to 1.0 V vs. RHE. The chronoamperometric test (*i-t*) was adopted at a constant potential 0.8 V vs. RHE to record the variation of current density. The anti-methanol test was carried out during the *i-t* process by injecting 10 mL methanol into the O_2-saturated 0.1 M KOH electrolyte. The double-layer capacitance (C_{dl}) was evaluated by CV measurements from 20 to 100 mv s^{-1} scan rates. TOF values were obtained via the following equation, where J is the measured current density, A accounts for the surface area of the electrode, 4 stands for the number of electrons transferred during O_2 reduction, m is the mole number of active sites, and F represents the Faraday constant (F = 96,485 C mol^{-1}).

$$TOF = \frac{j \times A}{4 \times m \times F} \tag{1}$$

The electrochemical OER tests were performed in 1.0 M KOH solution with automatic 95% iR compensation and the *i-t* test was continued at the constant 10 mA cm^{-2}.

1.5 Zn–Air Battery Assembly

Liquid-state ZABs were assembled with 6 M KOH and 0.2 M $Zn(CH_3COO)_2$ as the electrolyte, zinc plate as the anode, and Fe_2N_6-CMPCFs membrane (Loading: 1.5 mg cm^{-2}-2 mg cm^{-2}) as the cathode. Besides, Ni foam and hydrophobic carbon paper were used as the current collector and gas diffusion layer, respectively. The discharge and charge polarization curves were conducted at a scan rate of 5 mV s^{-1} on CHI-760E. The power density is obtained from the discharge polarization curve. The long-term stability tests were recorded with 20 min per cycle (10 min charge and 10 min discharge) on a Battery Testing System (NEWARE) at different temperatures (-10°C, 25°C, 50°C).

For flexible solid-state ZABs, KOH/sodium polyacrylate (KOH/PANa) hydrogel was prepared by the following process: 27 mL, 25 M sodium hydroxide solution was slowly added into acrylic acid solution (54 mL, 47 wt.%) under stirring in an ice bath for 12 h. Then, ammonium persulfate (0.78 g) was mixed into the above solution with ultrasonication for 0.5 h. After that, the polymerization process was proceeded at 40 °C for 30 h. Finally, the as-prepared PANa polymer was peeled off and fully dried and then soaked them into the 8M KOH and 0.2M $Zn(CH_3COO)_2$ solution overnight to obtain the KOH/PANa hydrogel.

1.6 Computational methods

This study employed the Vienna ab initio Simulation Package (VASP) code[2, 3] to conduct calculations based on density functional theory (DFT). The Perdew–Burke–Ernzerhof (PBE) functional[4] was utilized to describe the exchange-correlation energy within the generalized gradient approximation (GGA). The ionic cores were represented using projector augmented-wave (PAW) pseudo-potentials[5], and a plane wave cutoff energy of 500 eV was applied. To simulate electrocatalytic reactions, an implicit solvation model was employed using VASPsol[6], assuming a default relative permittivity of 78.4 F/m for water. Spin polarization was considered in all calculations. The electronic minimization process was done with a blocked Davidson iteration scheme. The self-consistent field (SCF) iteration converged with a threshold of 10^{-5} eV, and a Gaussian smearing of 0.05 eV was applied. Geometric optimization utilized a convergence threshold of 0.02 $eV·Å^{-1}$ for maximum force. A Γ-centered scheme was used for sampling k-points in the first Brillouin zone, with 2×2×1 k-points. To account for strong correlation repulsion between d-electrons with opposite spin in transition metal atoms, the DFT+U method was implemented[7], with an effective U value of 3.29 eV assigned to the Fe d-orbital[8]. The active site models were derived from modifying the p(7×6) graphene supercell model. A vacuum layer of 15 Å was incorporated in all models to mitigate the effects of periodic boundary conditions.

This study was built upon the overpotential theory established by Nørskov's research team[9]. Regarding the electrocatalytic oxygen reduction reaction (ORR) in solution, the reaction pathway can be described as follows:

$O_2 + {}^* + (H^+ + e^-) \rightarrow OOH^*$

$OOH^* + (H^+ + e^-) \rightarrow O^* + H_2O$

$O^* + (H^+ + e^-) \rightarrow OH^*$

$OH^* + (H^+ + e^-) \rightarrow H_2O + {}^*$

Adsorption free energy of various oxygen intermediates:

$\Delta G_{OOH*} = \Delta G(2H_2O(l) + {}^* \rightarrow OOH^* + 3/2H_2(g)) = \mu_{OOH*} + 1.5\mu_{H_2} - 2\mu_{H_2O} - \mu_*$

$\Delta G_{O*} = \Delta G(H_2O(l) + {}^* \rightarrow O^* + H_2(g)) = \mu_{O*} + \mu_{H_2} - \mu_{H_2O} - \mu_*$

$\Delta G_{OH*} = \Delta G(H_2O(l) + {}^* \rightarrow OH^* + 1/2H_2(g)) = \mu_{OH*} + 0.5\mu_{H_2} - \mu_{H_2O} - \mu_*$

Gibbs free energy change for each step of the ORR reaction:

$\Delta G_1 = \Delta G_{OOH*} - 4.916eV$

$\Delta G_2 = \Delta G_{O*} - \Delta G_{OOH*}$

$\Delta G_3 = \Delta G_{OH*} - \Delta G_{O*}$

$\Delta G_4 = - \Delta G_{OH*}$

Thermodynamic onset and over potential of ORR:

$U_{ORR}^{onset} = - \max\{\Delta G_1, \Delta G_2, \Delta G_3, \Delta G_4\}/e$

$U_{ORR}^{over} = 1.229\ V - U_{onset}$

For Fe_2N_6-based diatomic catalysts, due to the synergistic effect, OOH* exists in the form of OH-O*, while O* exists in the form of OH-OH*[10].

In the field of single-atom and diatomic electrocatalysis, in addition to having good thermodynamic intrinsic activity, the stability of the electrocatalyst is also crucial. The limited solubility of central metal ions is a necessary guarantee for maintaining the stability of catalysts.

To calculate the free energy of dissolution of the central metal ion, we design the following thermodynamic process:

Total process: Fe-N-C + $2H_2O \rightarrow H_2$-N-C + Fe^{2+} + $2OH^-$

Sub process: ①Fe-N-C + $2H_2O \rightarrow H_2$-N-C + $Fe(OH)_2$

②$Fe(OH)_2 \rightarrow Fe^{2+} + 2OH^-$

The free energy of process 1 was calculated by VASP based on density functional theory. H_2O and $Fe(OH)_2$ are considered as crystals. The free energy of process 2 could be obtained by using the thermodynamic formula "ΔG = -RTlnK", based on the conversion of the solubility product constant of $Fe(OH)_2$ (pKsp($Fe(OH)_2$) = 16.31)

The summation of the free energies of the two processes gives the free energy of the overall reaction, and higher stability of the central metal ion in the canonical center, the more positive free energy of the overall reaction.

Thermal corrections for adsorbed species, small molecules and post-processing of electronic structure analysis were based on VASPKIT[11].

The d-band centers (ε_d) were calculated from the density of states (DOS, $n_d(\varepsilon)$) using the following formula:

$$\varepsilon_d = \frac{\int_{-\infty}^{\infty} n_d(\varepsilon)\varepsilon d\varepsilon}{\int_{-\infty}^{\infty} n_d(\varepsilon) d\varepsilon}$$

The computation of crystal orbital Hamilton population[12, 13] (COHP) and partial charges, along with the projection of COHP onto each orbital, was performed by utilizing LOBSTER[14, 15].

-ICOHP represents the negative value of the integration of COHP from negative infinity to the Fermi energy:

$$-ICOHP = -\int_{-\infty}^{E_f} COHP(\varepsilon) d\varepsilon$$

2. Supplementary figures

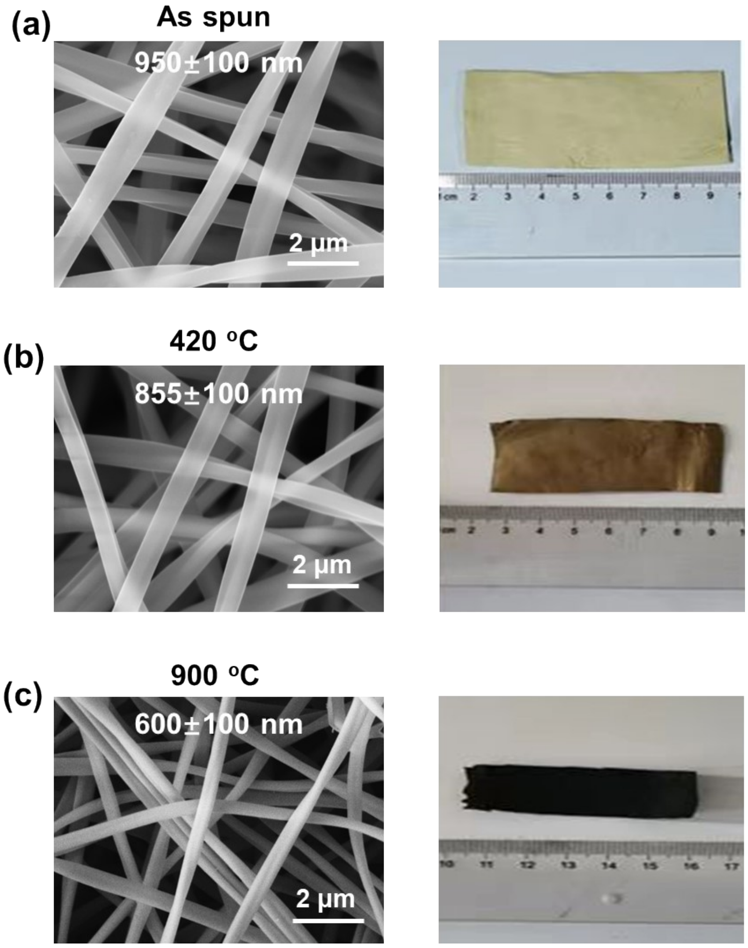

Figure S1. SEM images of a) as-spun fibers, b) fibers after heat treatment at 420℃, and their corresponding digital pictures.

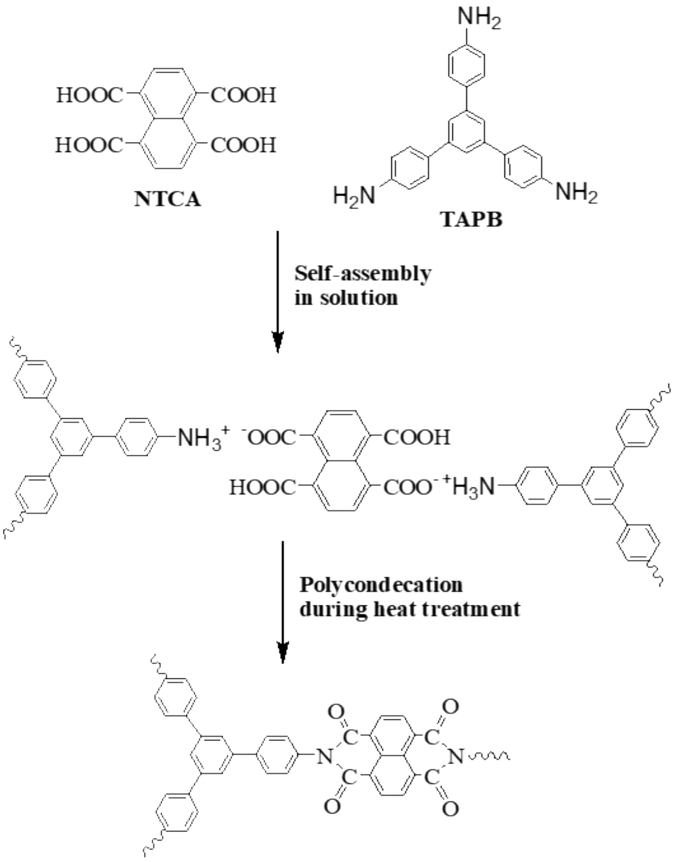

Figure S2. Chemical reaction equation of TAPB and NTCA.

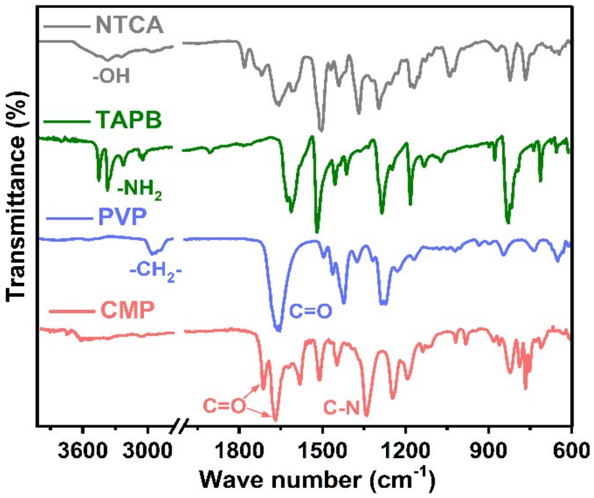

Figure S3. FTIR spectra of NTCA, TAPB, PVP, and CMP.

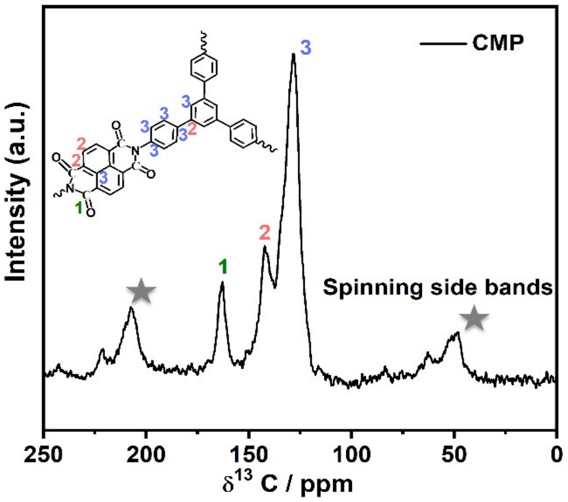

Figure S4. ^{13}C NMR spectra spectrum of CMP.

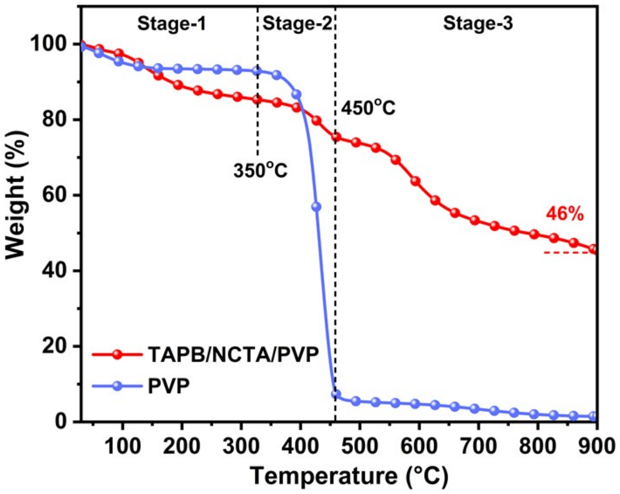

Figure S5. TGA curves of TAPB/NTCA/PVP and PVP.

Note: The weight loss of 15 wt.% in the first stage (25 to 350 ℃) can be attributed to the loss of H_2O, generating from the polycondensation of NTCA and TAPT. In addition, in the second stage (350 to 450 ℃), the weight loss of 9 wt.% can also be observed which is derived from the PVP decomposition. When further heating to 900 ℃, the TGA analysis exhibits a high carbon yield of 46% for our well-designed membrane.

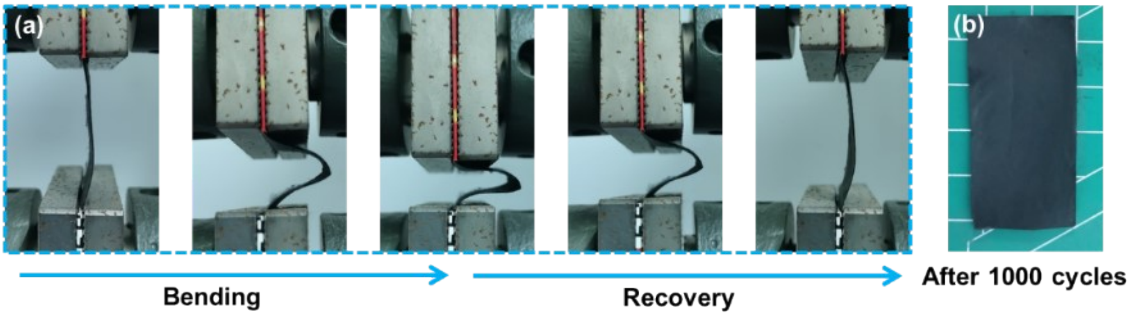

Figure S6. Bend testing for our as-prepared membrane.

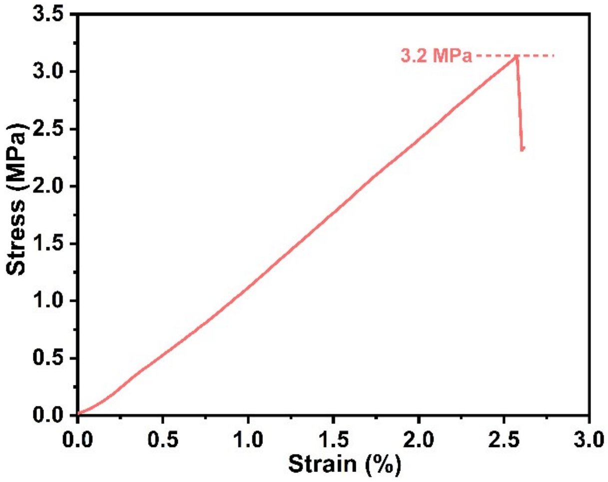

Figure S7. Tensile testing for our as-prepared membrane.

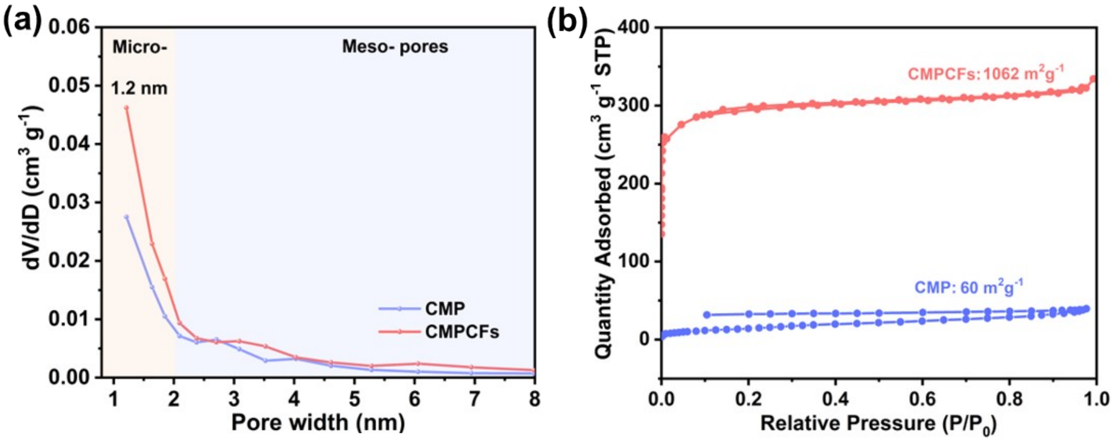

Figure S8. a) Pore size distribution of CMP and CMPCFs. b) Nitrogen adsorption-desorption isotherms of CMPCFs and CMP.

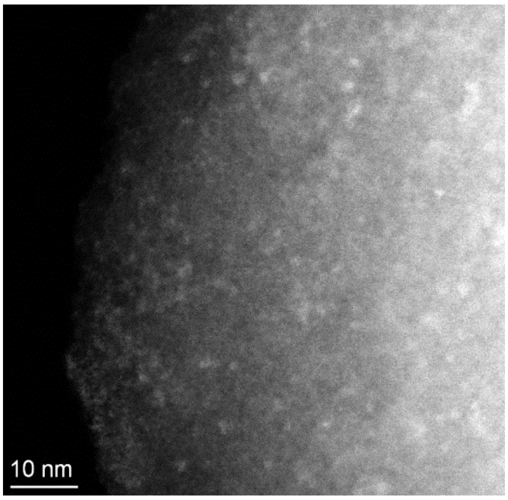

Figure S9. Aberration-corrected HAADF-STEM images of our sample after the first-step pyrolysis

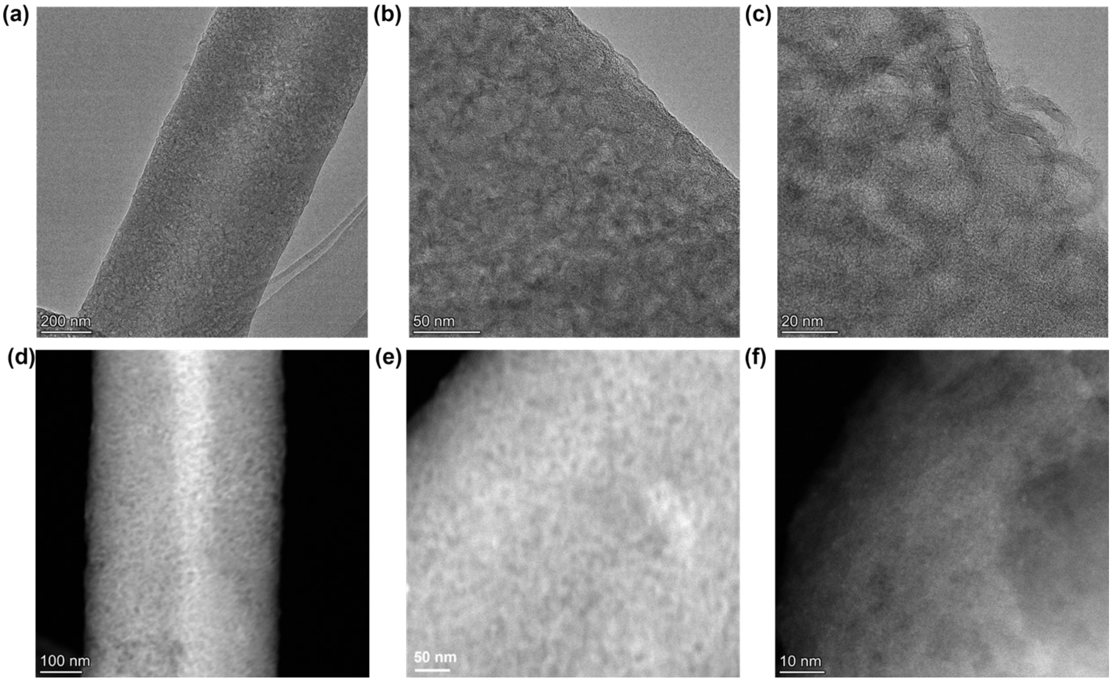

Figure S10. (a-c) TEM and (d-f) HAADF-STEM images of resultant Fe_2N_6-CMPCFs.

Note: TEM and HAADF-STEM images in different scales demonstrate that the Fe clusters is absent after the two-step NH_3-assisted pyrolysis.

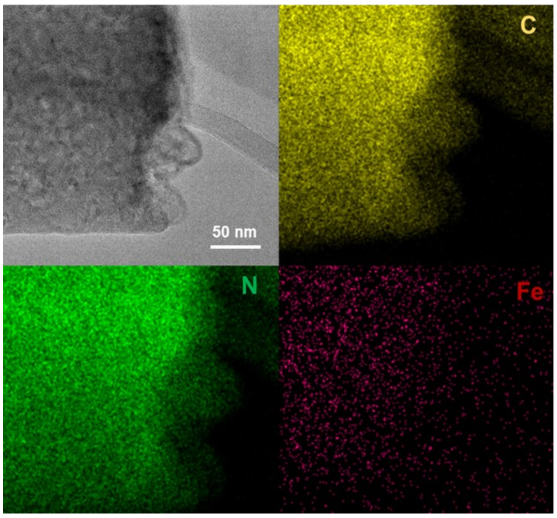

Figure S11. The energy-dispersive X-ray spectroscopy (EDS) images of Fe_2N_6-CMPCFs.

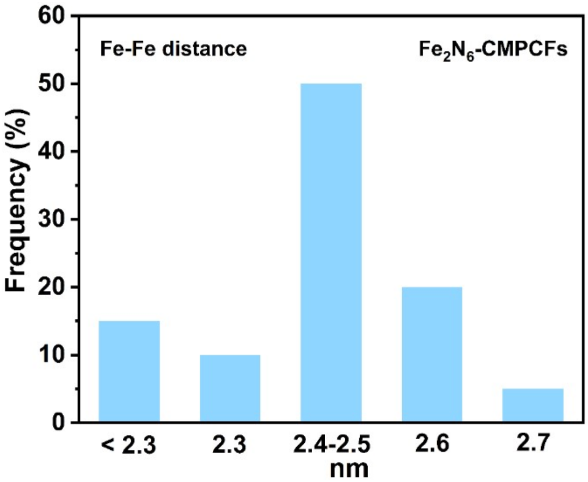

Figure S12. Statistical distribution of dual Fe-Fe distance in Fe_2N_6-CMPCFs.

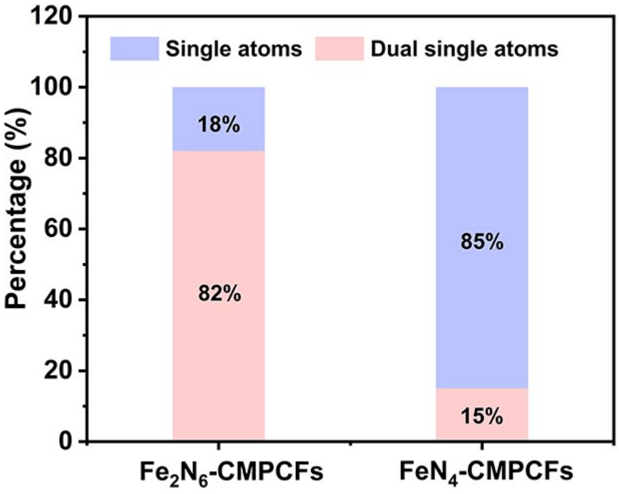

Figure S13. Statistical distribution of single-atomic and dual-single-atomic sites in FeN_4-CMPCFs and Fe_2N_6-CMPCFs.

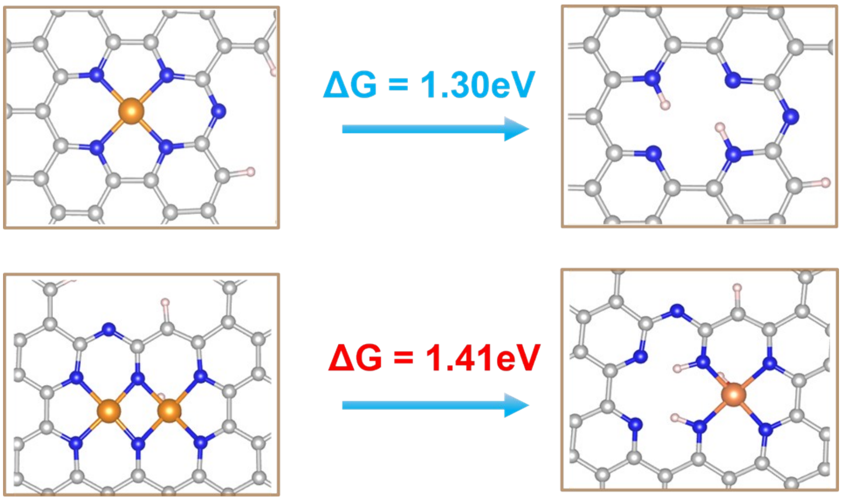

Figure S14. The diagram of the Fe atom dissolving from the carbon host into the solvent for FeN_4 and Fe_2N_6 structure. The orange, blue, gray, and pink balls represent the Fe, N, C, and H atoms respectively.

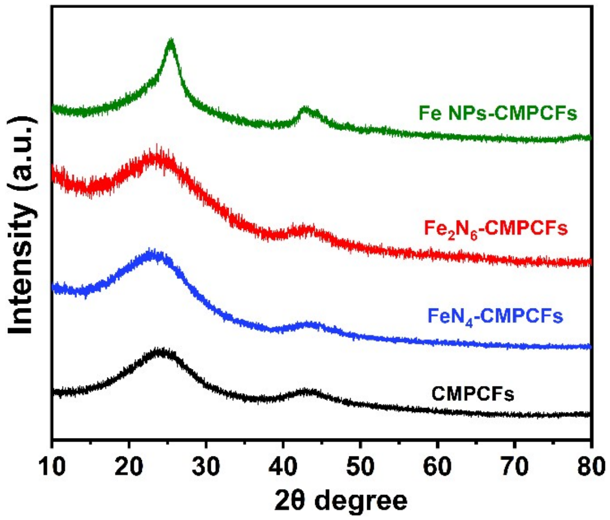

Figure S15. XRD patterns of FeN_4-CMPCFs, Fe_2N_6-CMPCFs, Fe NPs-CMPCFs, and CMPCFs.

Note: XRD did not detect any crystalline Fe species in FeN_4-CMPCFs and Fe_2N_6-CMPCFs. While, for Fe NPs-CMPCFs sample, a tiny peak at 44°corresponds to the (110) facet of metallic iron, illustrating the existence of Fe aggregation.

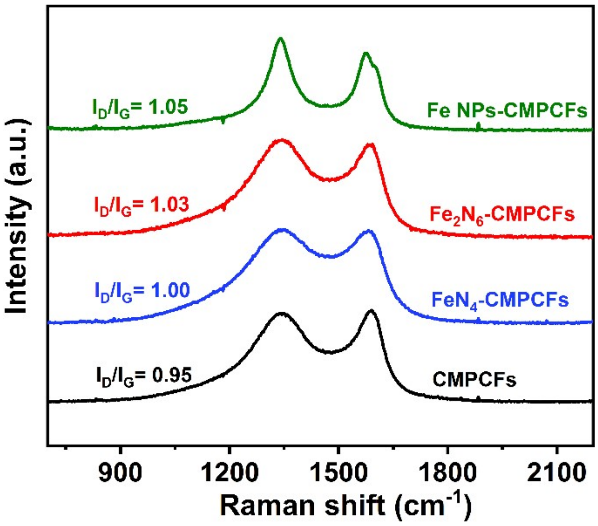

Figure S16. Raman spectra of FeN_4-CMPCFs, Fe_2N_6-CMPCFs, and Fe NPs-CMPCFs, CMPCFs.

Note: With increasing the Fe dopant, the degree of carbon defect gradually increased.

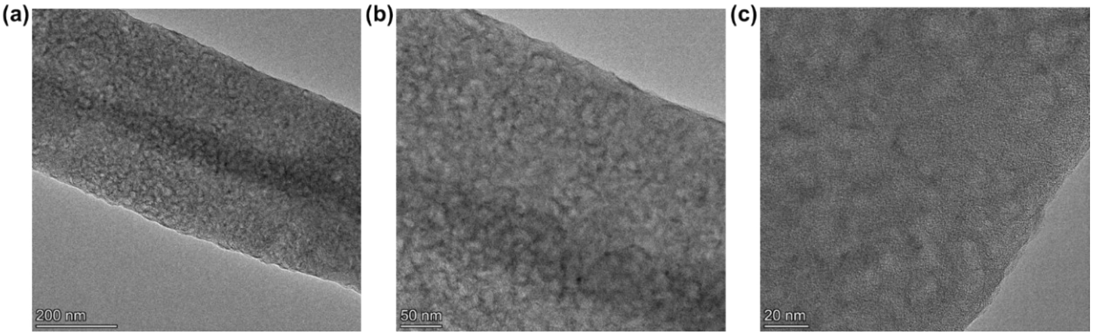

Figure S17. TEM images of FeN$_4$-CMPCFs.

Note: TEM cannot detect any Fe aggregation of FeN$_4$-CMPCFs sample.

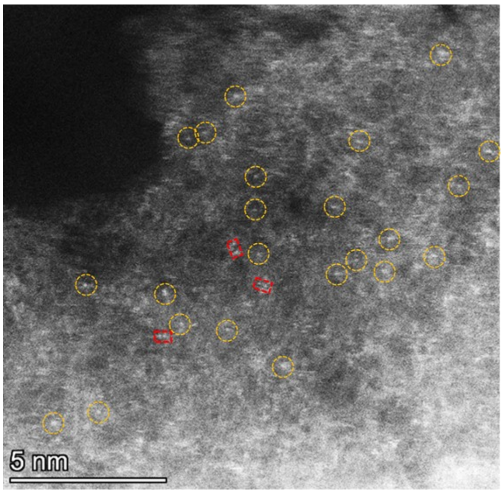

Figure S18. The AC-HAADF-STEM image of FeN$_4$-CMPCFs.

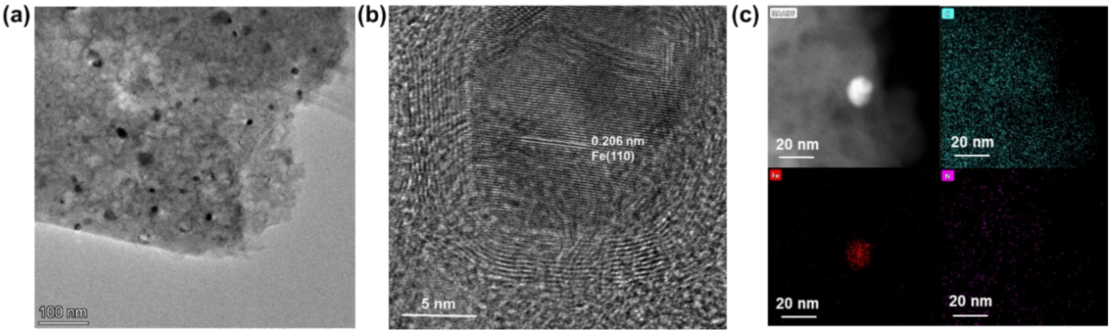

Figure S19. a-b) TEM images of Fe NPs-CMPCFs. c) HAADF-STEM image and its corresponding EDS mappings.

Note: Obvious metal nanoparticles can be seen in Fe NPs-CMPCFs. According to its lattice spacing and EDS mapping, we conclude that its metal aggregation belongs to the Fe nanoparticles. Meanwhile, we can also observe the graphitic carbon layer in Figure S18b, which is consistent with the XRD result in Figure S14.

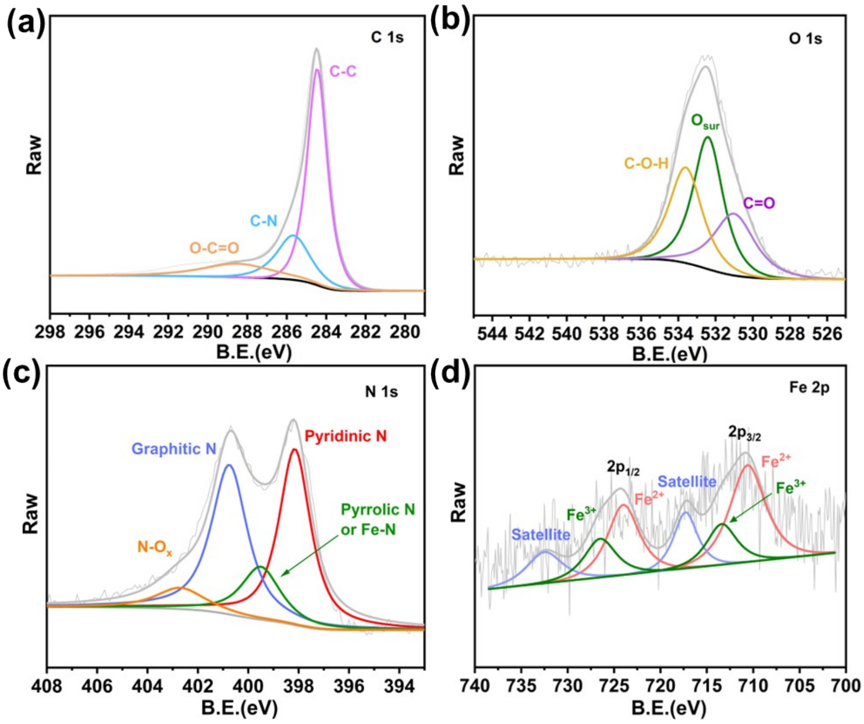

Figure S20. High-resolution XPS spectra of C 1s, O 1s, N 1s and Fe 2p for FeN$_4$-CMPCFs.

Note: Compared with Fe-CMPCFs-Ar, the ratio of pyridinic-N increases sharply in FeN$_4$-CMPCFs.

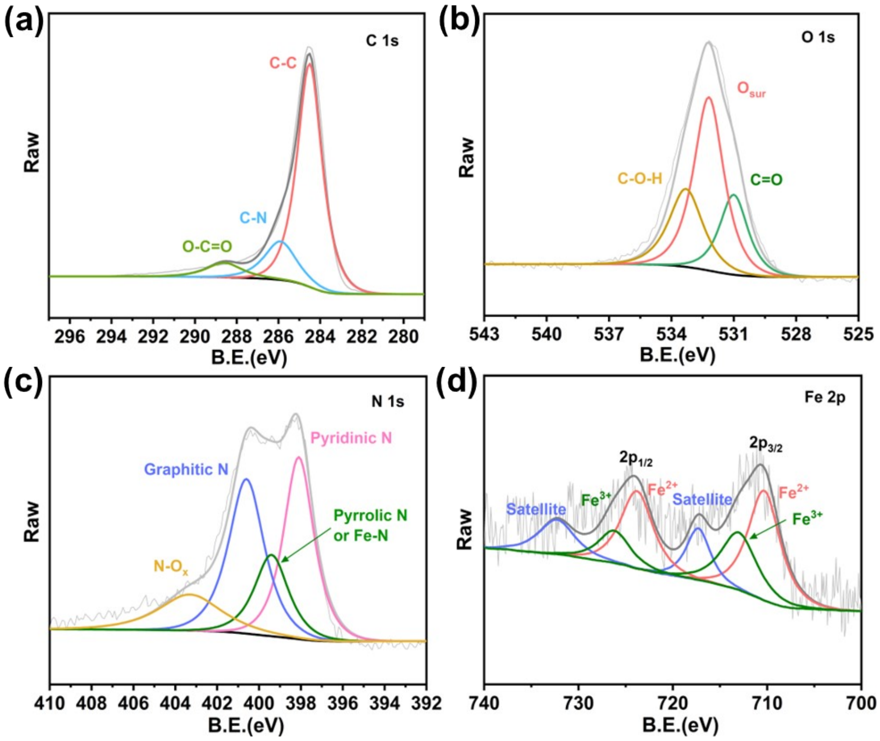

Figure S21. High-resolution XPS spectra of C 1s, O 1s, N 1s and Fe 2p for Fe_2N_6-CMPCFs.

Note: The percentage of pyrrolic-N or Fe-N obviously rises in Fe_2N_6-CMPCFs.

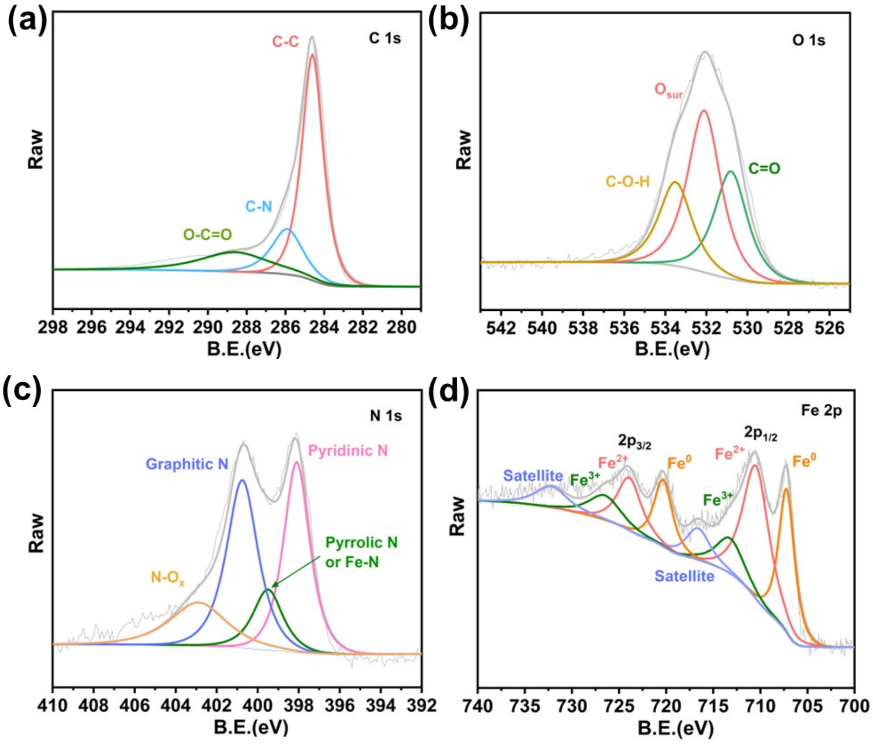

Figure S22. High-resolution XPS spectra of C 1s, O 1s, N 1s and Fe 2p for Fe NPs-CMPCFs.

Note: For Fe NPs-CMPCFs, a distinct peak at around 706 eV in Fe 2p spectrum represents the existence of Fe nanoparticles.

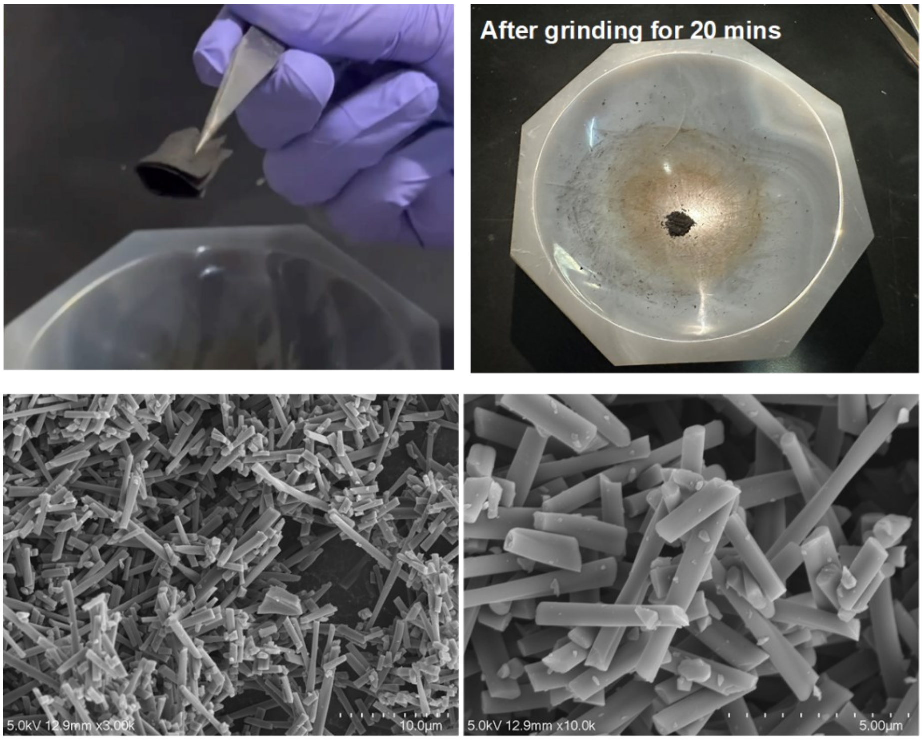

Figure S23. The digital pictures and SEM images of the wrecked membrane for electrochemical tests.

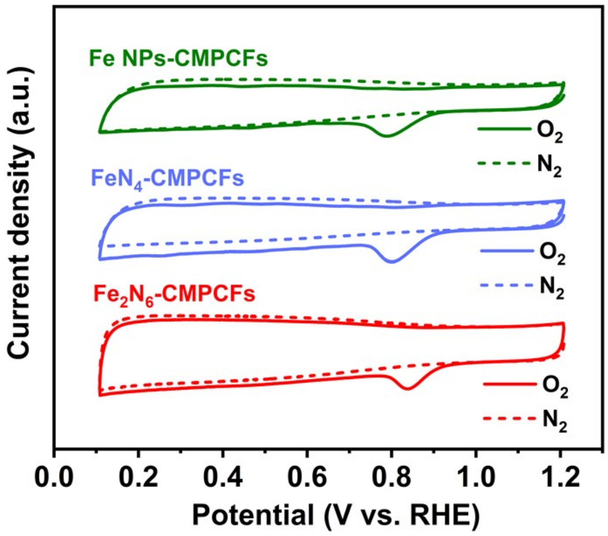

Figure S24. CV curves of Fe2N6-CMPCFs, FeN4-CMPCFs, Fe NPs-CMPCFs in N_2- and O_2-saturated 0.1 M KOH at a scan rate of 50 mV/s with 0 rpm**.**

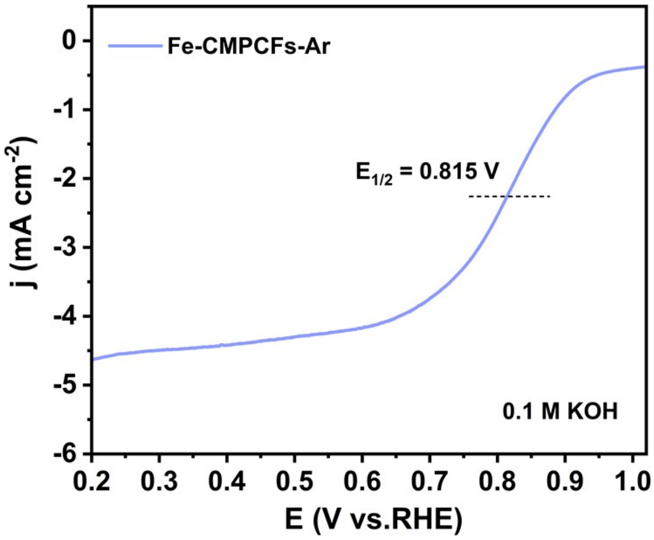

Figure S25. The LSV curve for the sample after first-step pyrolysis.

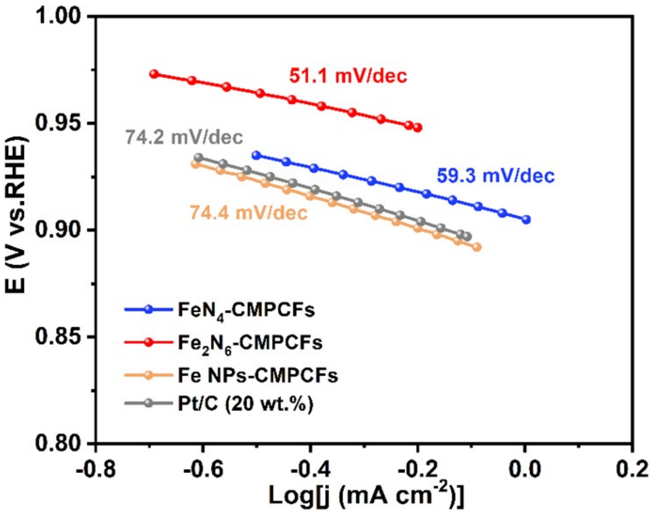

Figure S26. Tafel slope of FeN$_4$-CMPCFs, Fe$_2$N$_6$-CMPCFs, Fe NPs-CMPCFs and Pt/C.

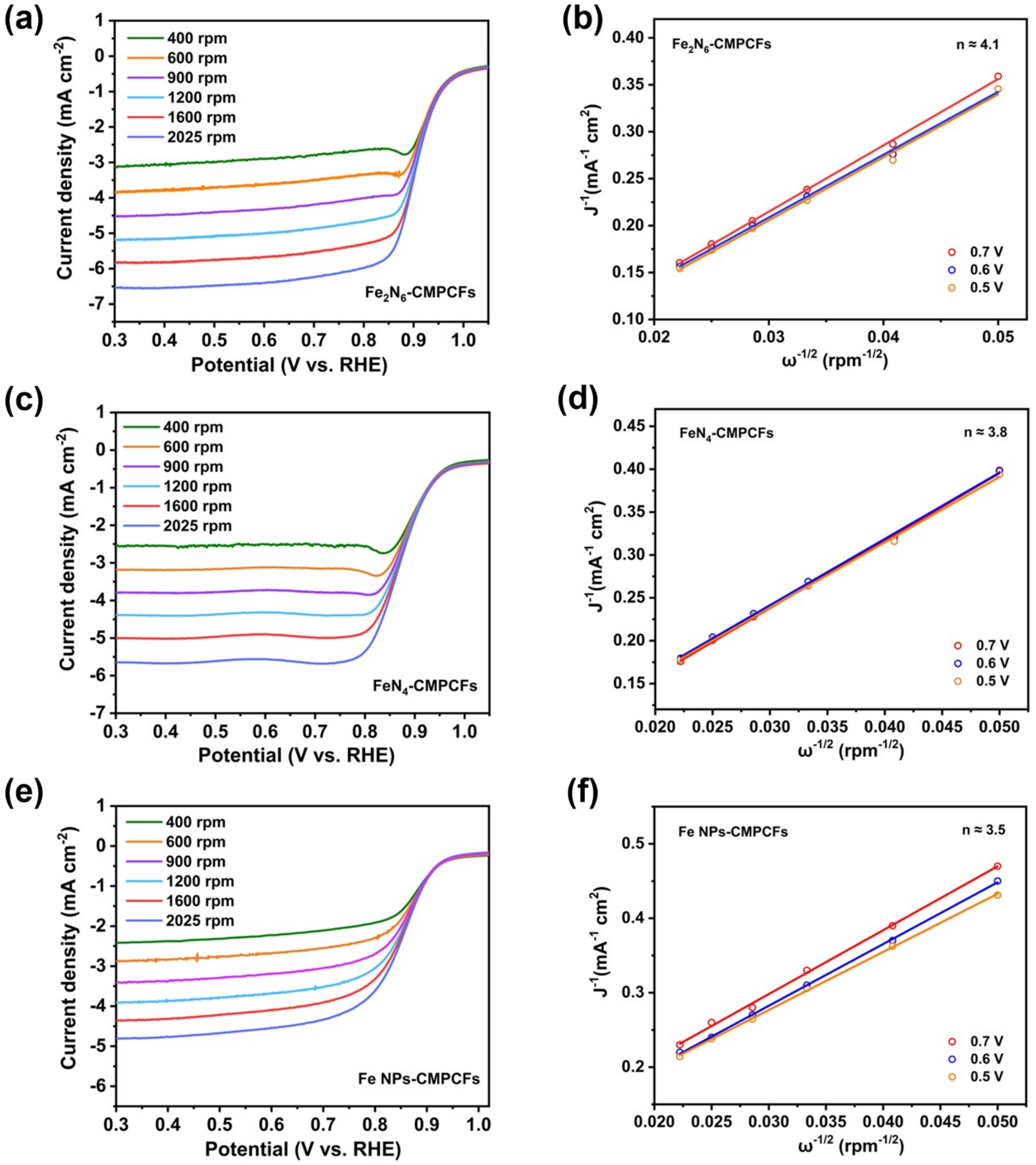

Figure S27. ORR linear sweeps with various rotating rates and K–L plots at different potentials in O_2-saturated 0.1 M KOH for (a-b) Fe_2N_6-CMPCFs, (c-d) FeN_4-CMPCFs, (e-f) Fe NPs-CMPCFs.

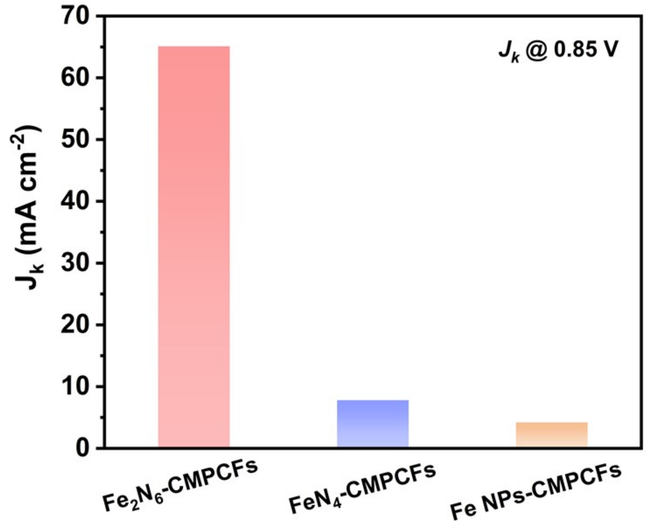

Figure S28. Kinetic current density (J_k) at 0.85 V for different catalysts.

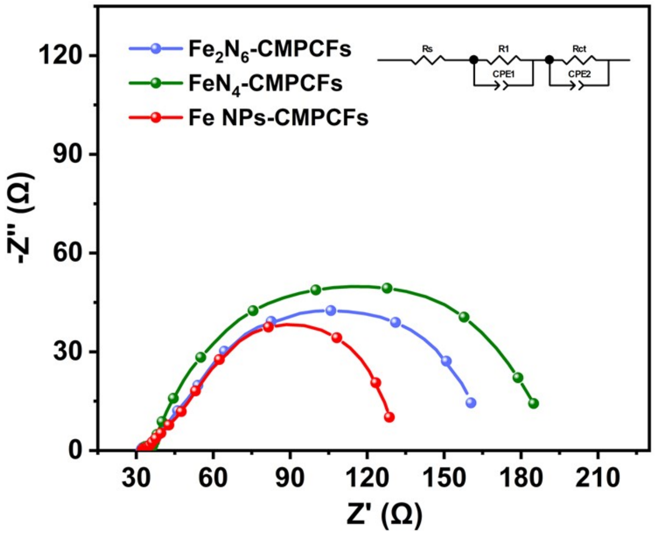

Figure S29. Electrochemical impedance spectra (EIS) of Fe_2N_6-CMPCFs, FeN_4-CMPCFs, and Fe NPs-CMPCFs catalysts with a rotation speed of 1600 rpm at the potential of 0.86 V vs RHE. (The insert is the equivalent circuit model).

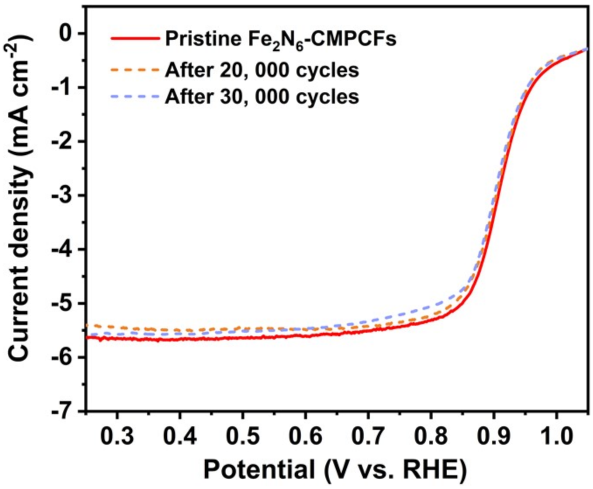

Figure S30. The LSV curves of Fe$_2$N$_6$-CMPCFs after 20, 000 and 30, 000 cycles.

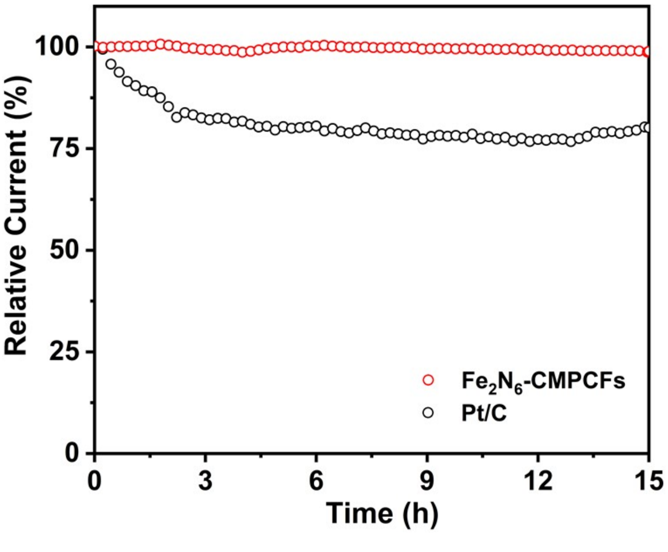

Figure S31. Chronoamperometry test (*i*-t) of Fe$_2$N$_6$-CMPCFs and Pt/C.

Note: *i*-t measurement shows Fe$_2$N$_6$-CMPCFs can remain nearly 98% original current, outperforming commercial Pt/C (65%) at 0.8 V vs. RHE.

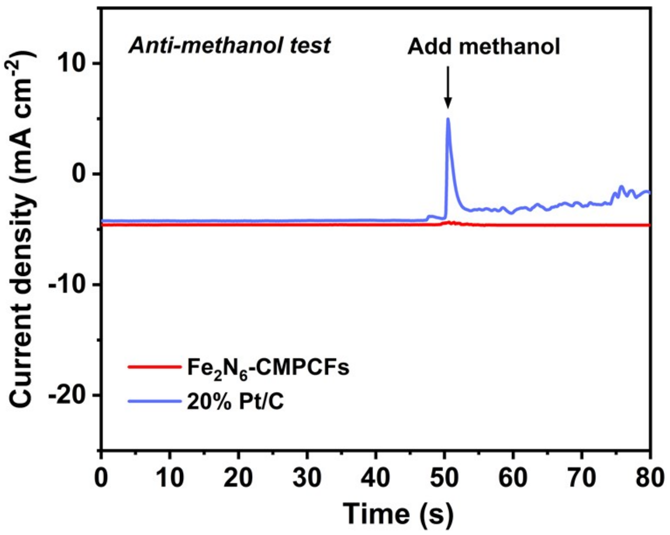

Figure S32. Methanol tolerance of Fe_2N_6-CMPCFs and Pt/C.

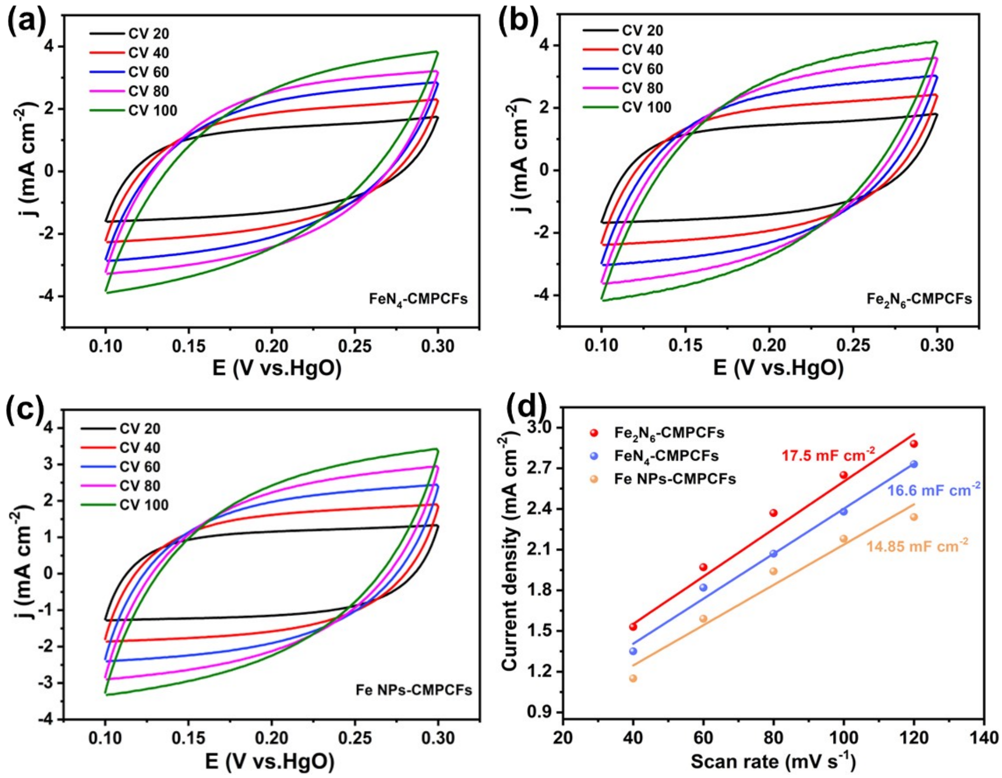

Figure S33. Cyclic voltammetry (CV) curves of a) FeN$_4$-CMPCFs, b) Fe$_2$N$_6$-CMPCFs, and c) Fe NPs-CMPCFs catalyst at different scan rates ranging from 40 to 120 mV s^{-1}. d) Capacitive currents versus scan rates of different samples.

Note: The double layer capacitance (C_{dl}) value was estimated by the linear slope of the fitted line which was plotted by capacitive currents versus scan rates. Herein, the scan rate was used from 40 to 120 mV s^{-1}.

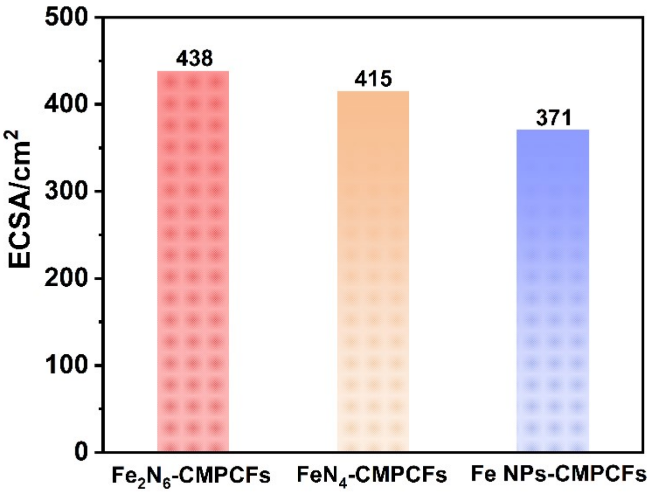

Figure S34. Bar chart of ECSA value for as-prepared catalysts.

Note: ECSA is determined through the following equation:

$$\text{ECSA} = \frac{Cdl}{Cs}$$

where the *Cs* value is adopted as ≈ 0.04 mF cm^{-2}.

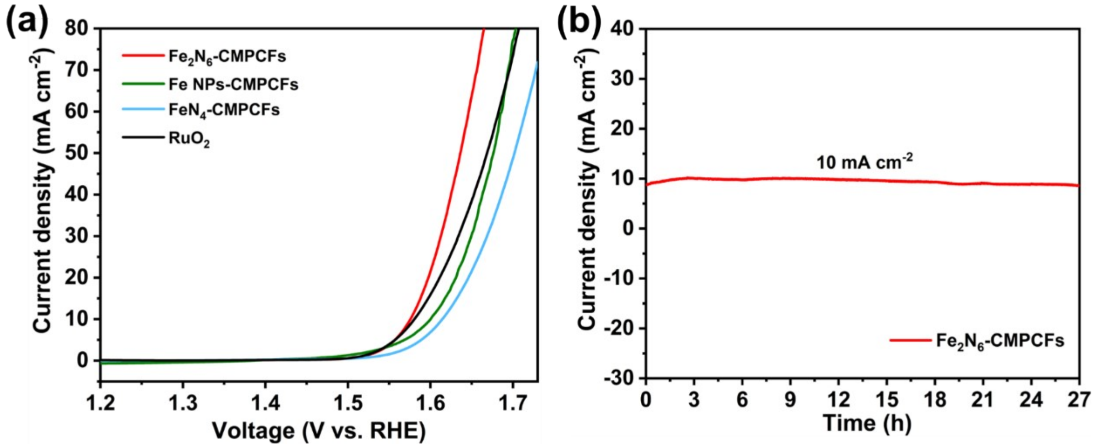

Figure S35. (a) LSV curves of Fe$_2$N$_6$-CMPCFs, FeN$_4$-CMPCFs, Fe NPs-CMPCFs and RuO2; (b) The *i-t* test of Fe$_2$N$_6$-CMPCFs.

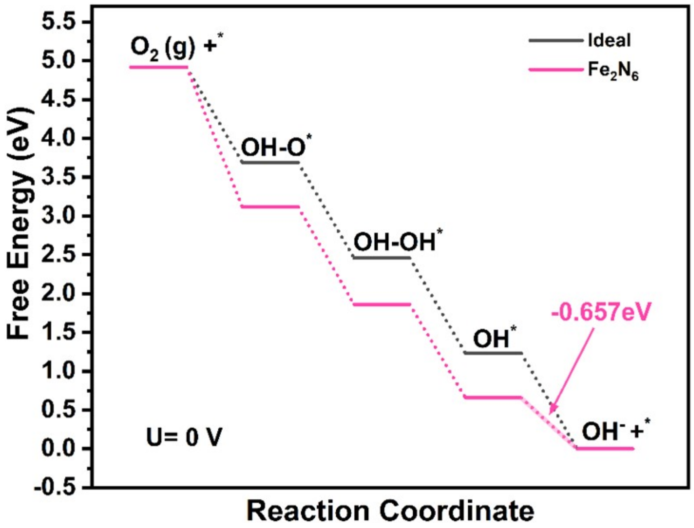

Figure S36. Free energy diagrams of the ORR on Fe_2N_6 structure.

Note: From the last step, we can observe that the calculated free energy is relatively low, which is always negative at the working potential. Therefore, Fe_2-N_6 sites trend to coordinate by an extra OH ligand (Fe_2N_6OH) when they serve as ORR active sites.

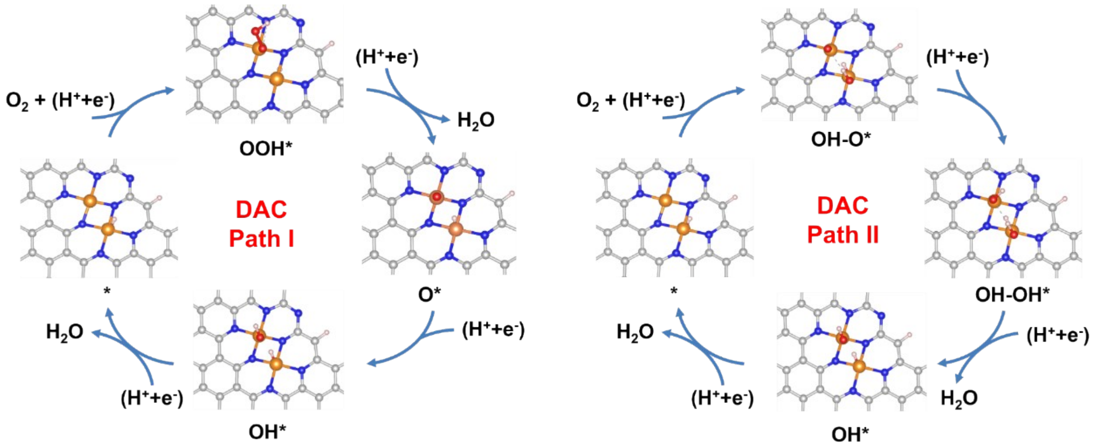

Figure S37. Reaction scheme of $Fe_2N_6OH\text{-}C_h\text{-}N_{py}$ sites in the traditional ORR pathway (Path I) and the two-site dissociation pathway (Path II).

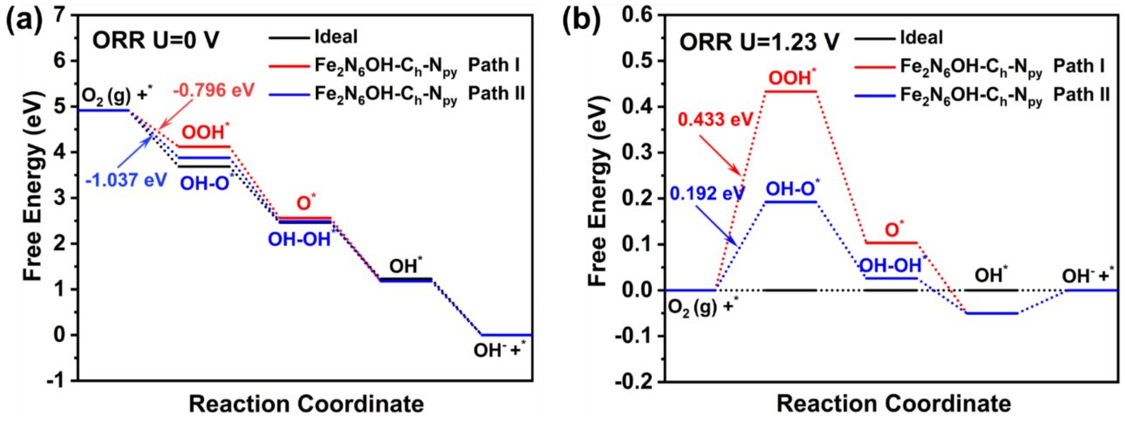

Figure S38. The Gibbs energy diagrams of Fe_2N_6OH-Ch-Npy sites (a) U=0V and (b) U= 1.23V in the traditional pathway (Path I) and the two-site dissociation pathway (Path II).

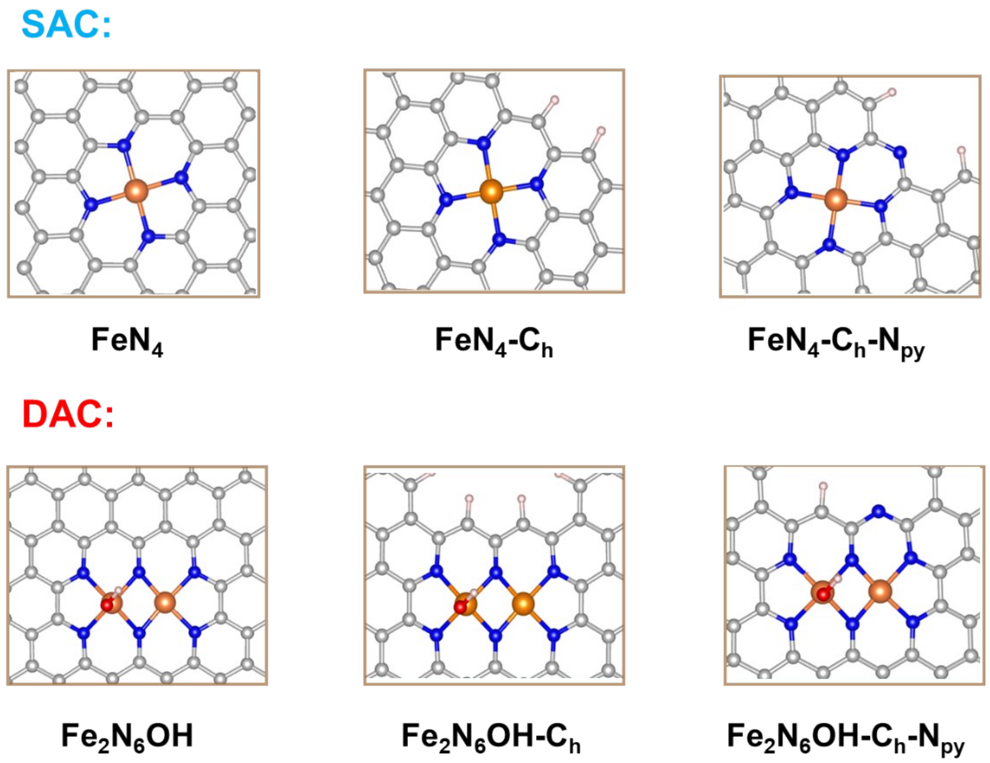

Figure S39. Structure diagrams of different SAC and DAC catalysts (the balls in brown, yellow, white, red, and pink represent C, Fe, N, O, H, respectively.).

Note: Here, C_h represents the existence of carbon holes around the active sites, and N_{py} represents the existence of pyridinic-N around the active sites.

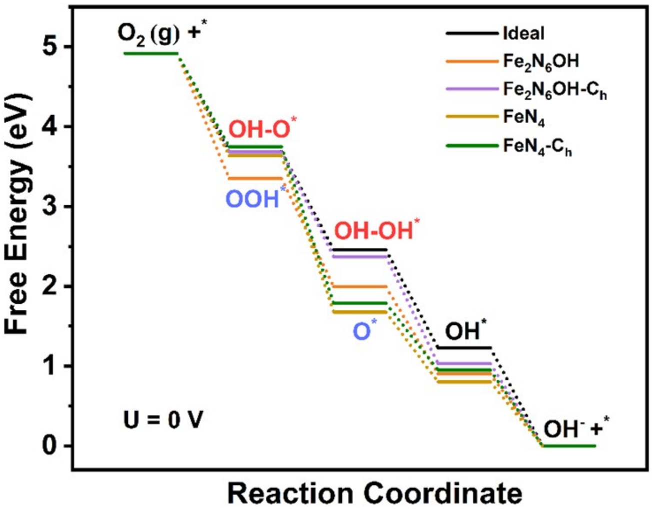

Figure S40. Free energy diagrams of the ORR on FeN_4, FeN_4-C_h, Fe_2N_6OH, and Fe_2N_6OH-C_h.

Note: We discover that the Fe_2N_6 system (Fe_2N_6OH, and Fe_2N_6OH-C_h) is closer to the ideal's free energy pathways of ORR at U=0 V, which reveals that the synergistic interaction between Fe-Fe in DAC system can facilitate the ORR catalytic reaction.

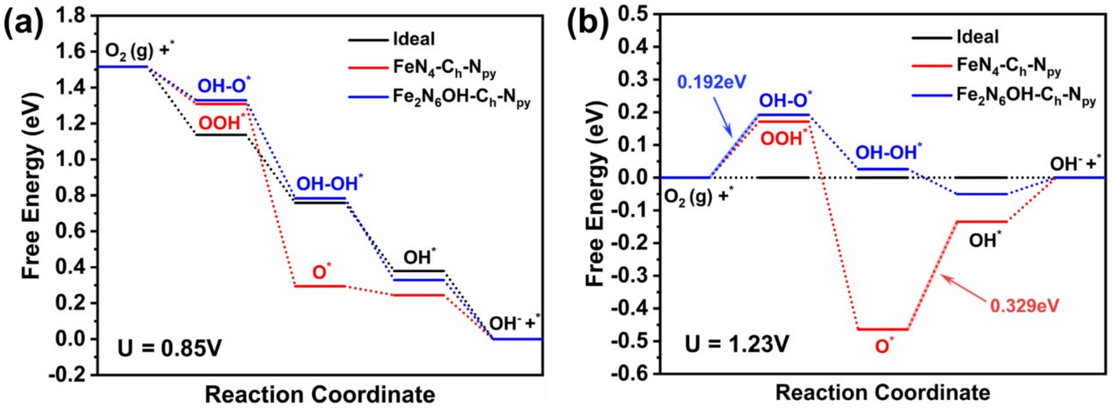

Figure S41. Free energy diagrams of the ORR on Fe$_2$N$_6$OH-C$_h$-N$_{py}$ at (a) U=1.23V and (b) U=0.85 V.

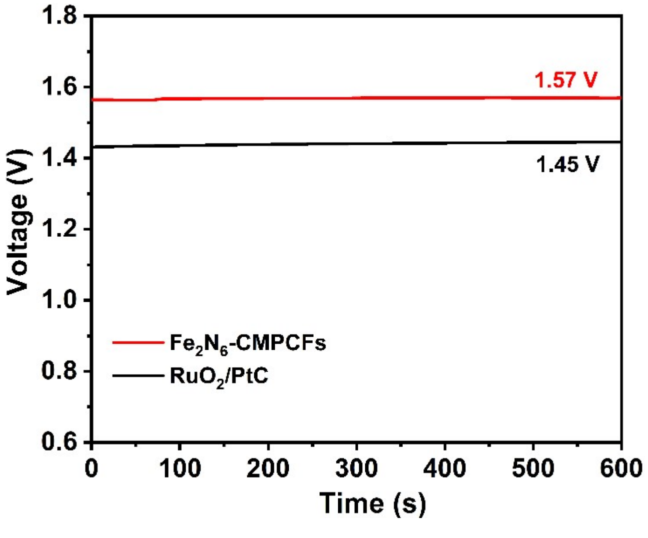

Figure S42. Open-circuit voltage of ZABs using Fe$_2$N$_6$-CMPCFs and RuO$_2$/PtC.

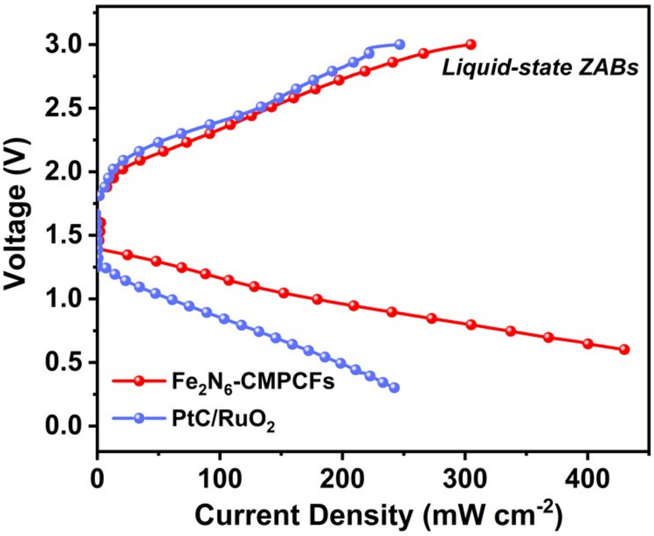

Figure S43. Charge/discharge polarization profiles of liquid-state ZABs by using Fe_2N_6-CMPCFs and PtC/RuO_2 as cathodes.

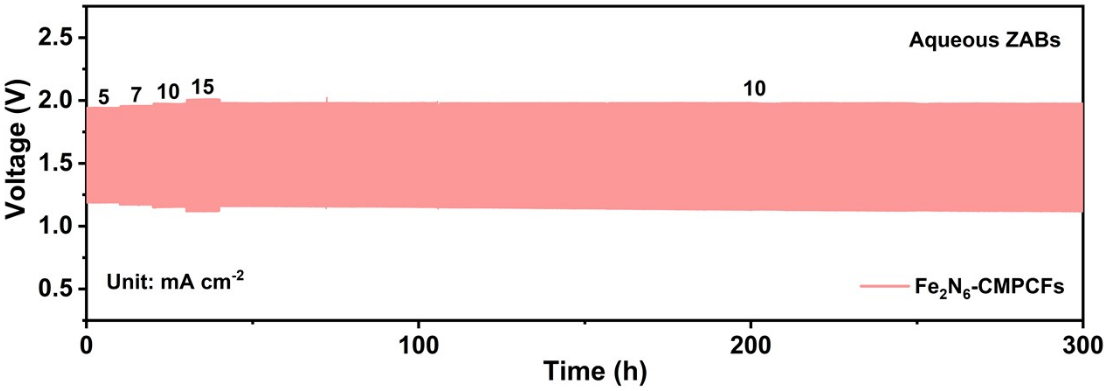

Figure S44. The rate capacity of liquid-state ZABs by using Fe_2N_6-CMPCFs at large current densities.

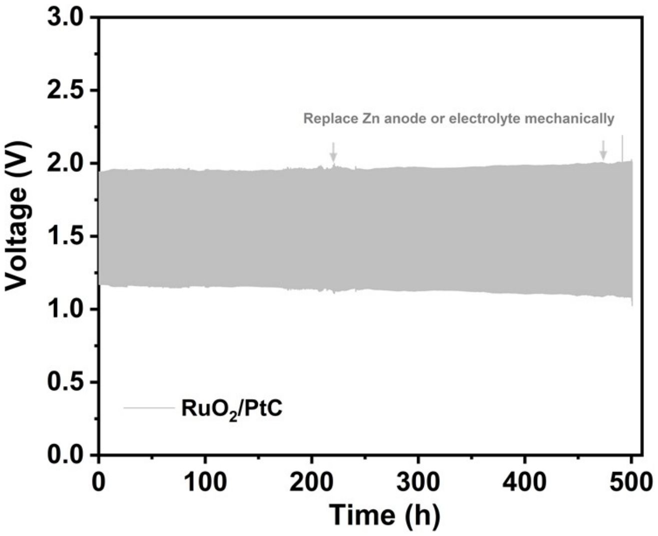

Figure S45. Galvanostatic discharge-charge test of RuO_2/PtC at 5 mA cm^{-2}.

Note: It is obvious that despite replacing the Zn anode and electrolyte, the voltage gap is still continuously increasing for RuO_2/PtC-based ZABs.

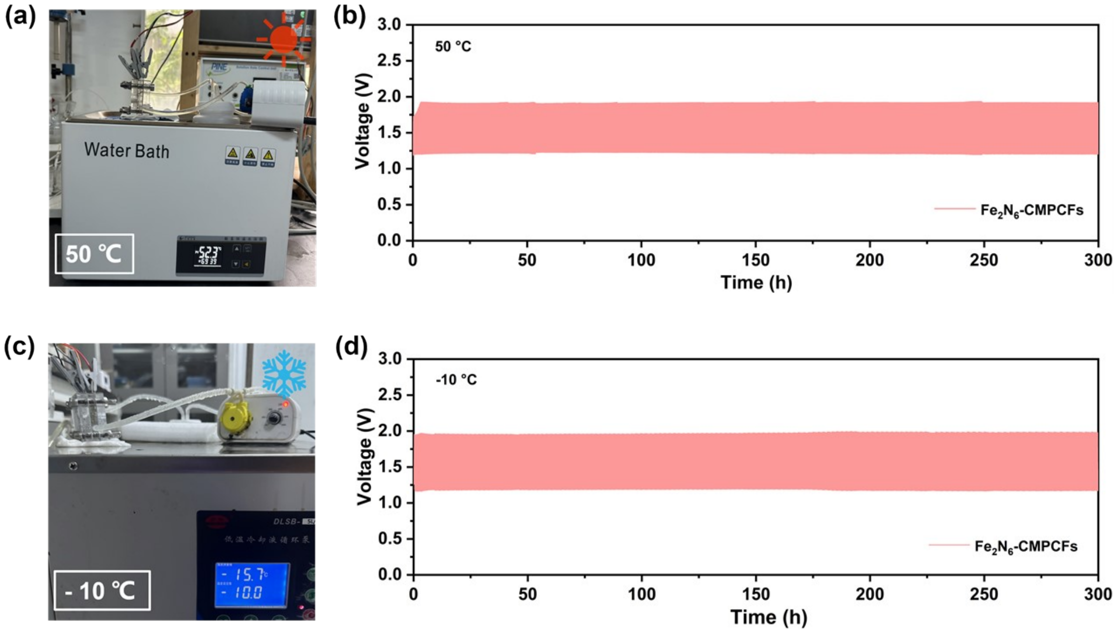

Figure S46. The stability tests of Fe_2N_6-CMPCFs membrane-based ZABs under (a) high temperature (50 °C) and (b) low temperature (-10 °C) conditions at 5 mA cm^{-2}.

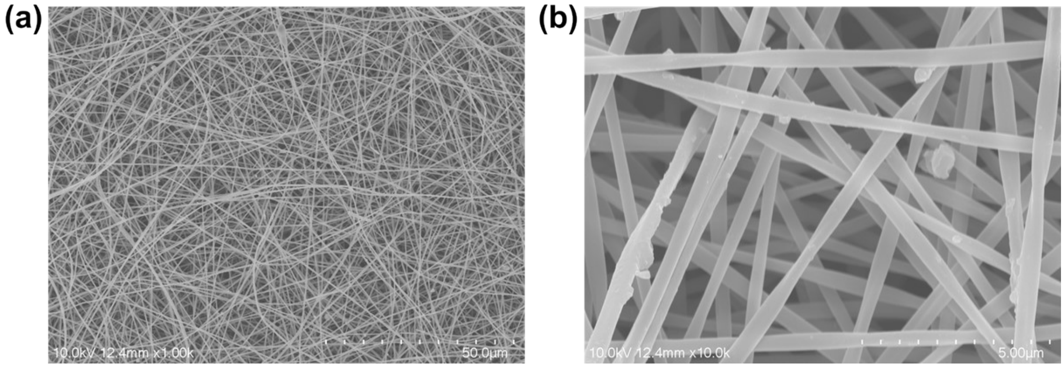

Figure S47. SEM images of Fe_2N_6-CMPCFs membrane after 4800-h battery operation.

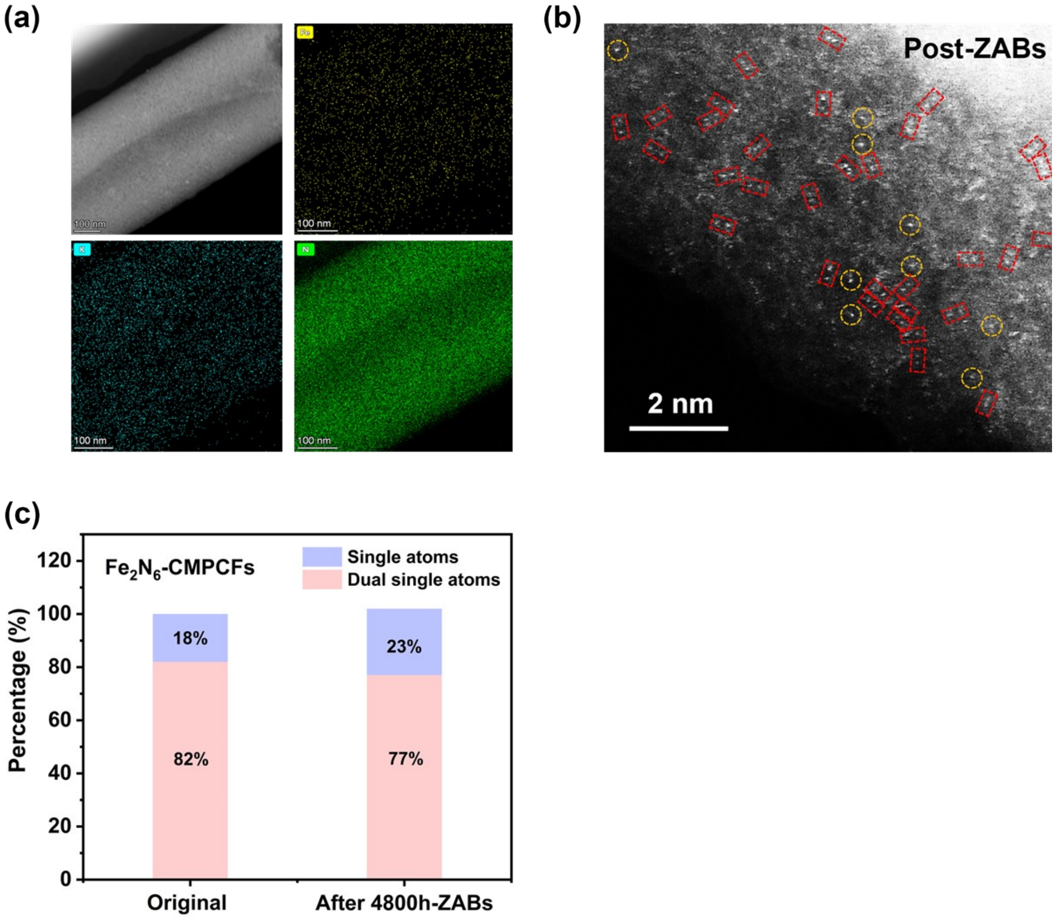

Figure S48. (a-b) AC-HAADF-STEM images of Fe_2N_6-CMPCFs after the discharge-charge cycling. (c) The statistical analysis of single-atomic and dual-atomic sites in Fe_2N_6-CMPCFs before and after the 4800-h cycling of ZABs.

Note: Based on HAADF-STEM images, the fibrous structure remains well-reserved without noticeable Fe aggregation. Notably, the high ratio of dual-single-atomic sites, up to approximately 77 %, can be detected after the 4800-h cycling, demonstrating its remarkable anti-dissolving effect.

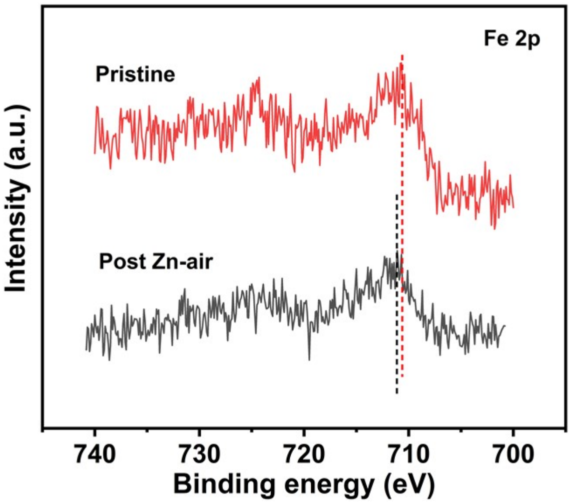

Figure S49. The Fe 2p XPS spectra of Fe_2N_6-CMPCFs before and after the cycling test.

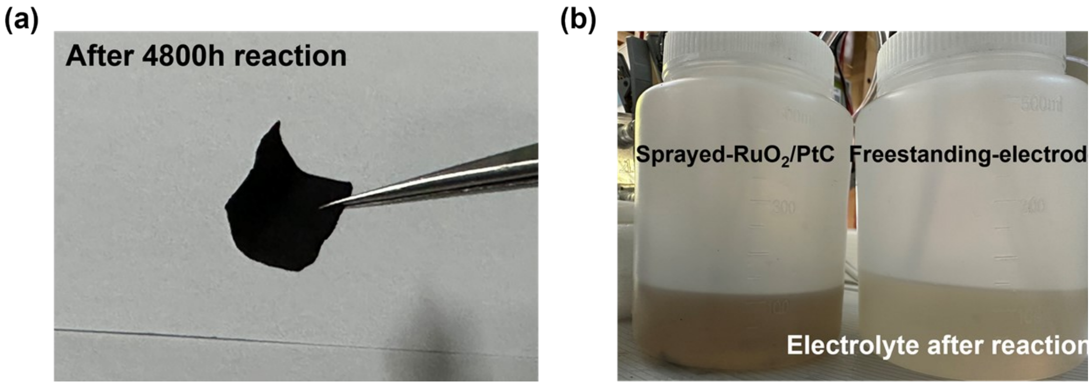

Figure S50. Digital photos of a) freestanding membrane and b) electrolyte after the cell operation.

Note: We can obviously see the color difference of electrolyte between sprayed-RuO$_2$/PtC and freestanding Fe$_2$N$_6$-CMPCFs membrane after long-term Zn-air operation, which illustrates the sprayed catalysts trend to peel off from the substrate during the cell operation. By contrast, the self-supporting integrated Fe$_2$N$_6$-CMPCFs membrane preserves perfectly after the 4800-h cell operation.

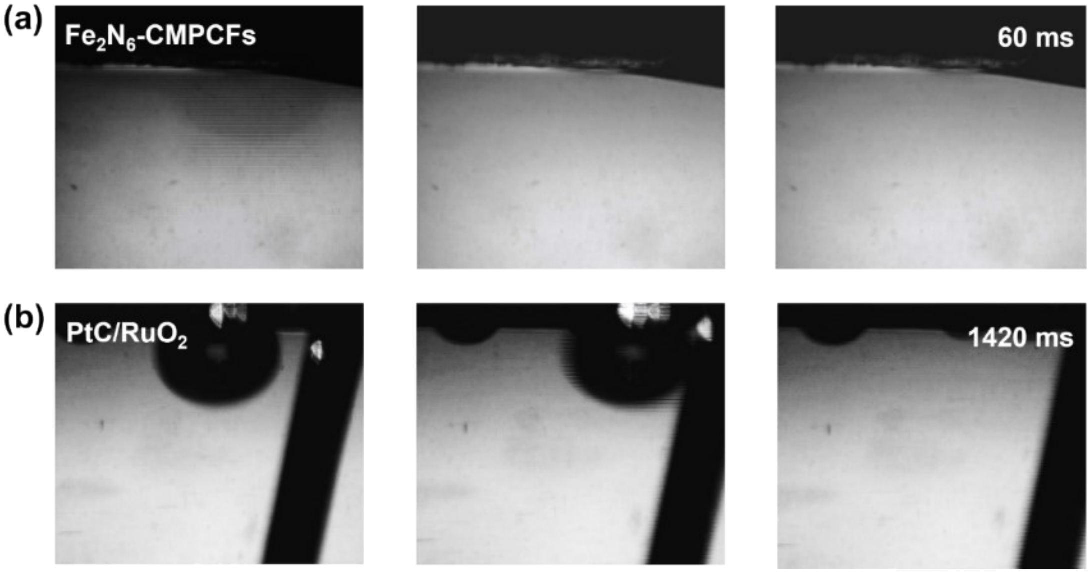

Figure S51. O_2 bubbles adhesion behavior evolution on the surfaces of PtC/RuO_2 and Fe_2N_6-CMPCFs membrane.

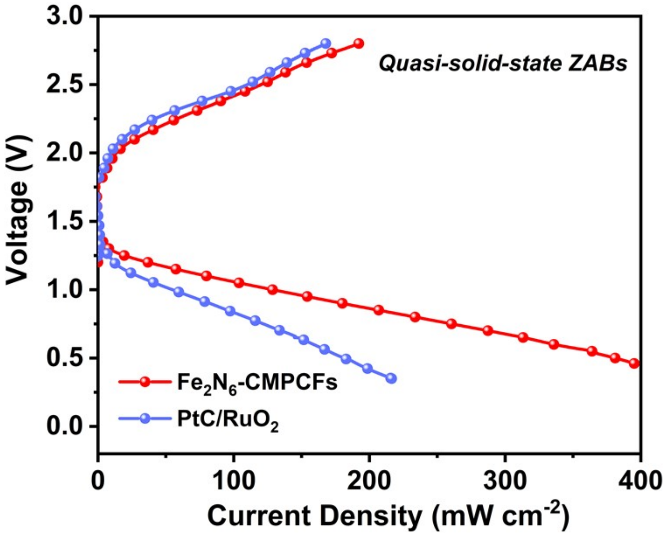

Figure S52. Charge/discharge polarization profiles of quasi-solid-state ZABs by using Fe_2N_6-CMPCFs and PtC/RuO_2 as cathodes.

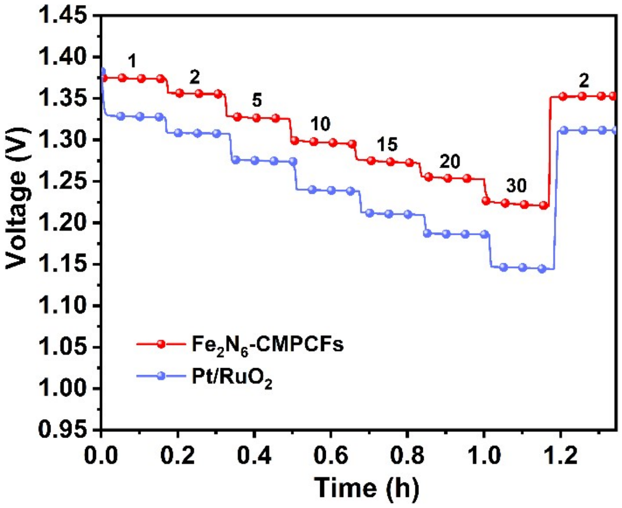

Figure S53. Rate performance of Fe_2N_6-CMPCFs and RuO_2/PtC based quasi-solid-state Zn-air batteries.

Note: Fe_2N_6-CMPCFs based solid-state Zn-air battery performs a higher voltage platform (1.23 V) than that of RuO_2/PtC (1.15 V) at the current density of 30 mA cm^{-2}.

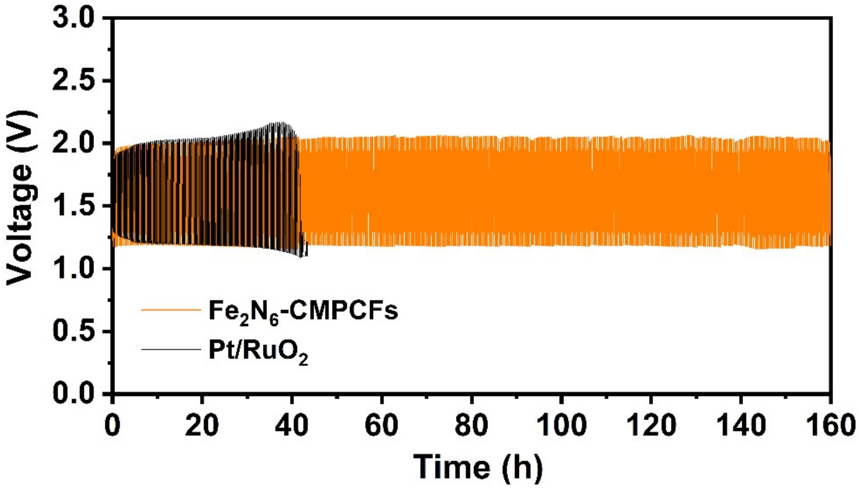

Figure S54. Galvanostatic discharging-charging test of flexible solid-state Fe_2N_6-CMPCFs-based ZABs.

Note: Without replacing the hydrogel, Fe_2N_6-CMPCFs based solid-state ZABs display better stability and long-cycling lifespan.

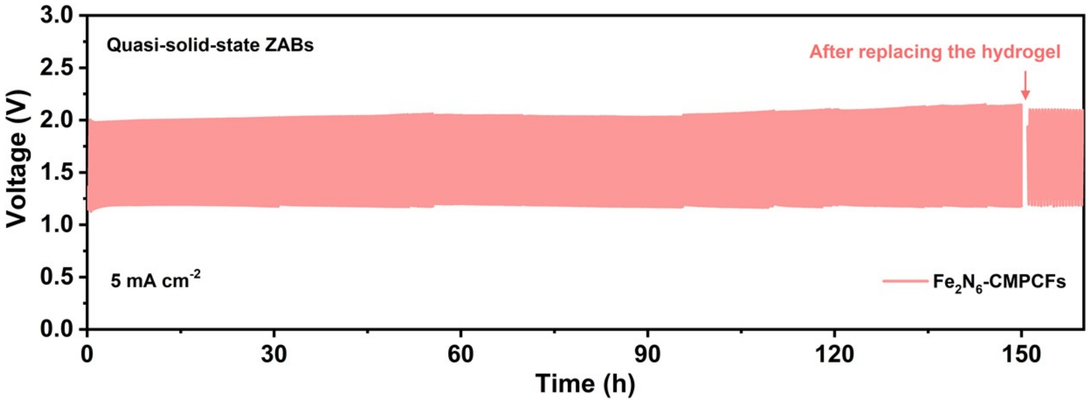

Figure S55. The stability test for quasi-solid-state ZABs by using Fe_2N_6-CMPCFs membranes at a higher current density of 5 mA cm^{-2}. The hydrogel is replaced after 150 h.

Figure S56. Optical photos of solid-state ZABs-driven LED screens.

3. Supplementary tables

Table S1. Dissolution Free energy of Fe atoms (ΔG_{disso}).

	ΔG_{disso}
FeN_4	0.94
FeN_4-C_h	1.30
FeN_4-C_h-N_{py}	1.32
Fe_2N_6-C_h-N_{py}	1.41

Table S2. Content of iron in different samples (tested by Inductively Coupled Plasma).

Catalyst	FeN_4-CMPCFs	Fe_2N_6-CMPCFs	Fe NPs-CMPCFs
Content (wt.%)	1.5	2.6	3.9

Table S3. The content of elements obtained from XPS analysis.

	C (wt.%)	N (wt.%)	O (wt.%)	Fe (wt.%)
FeN_4-CMPCFs	84.1	4.9	10.0	1.2
Fe_2N_6-CMPCFs	81.8	5.4	10.4	2.4
Fe NPs-CMPCFs	80.6	3.9	11.2	4.4

Table S4. Fitting parameters for Fe K-edge EXAFS for related samples.

	Shell	CN	R(Å)	σ^2	ΔE_0	R factor
Fe foil	Fe-Fe	8	2.47±0.01	0.0047	7.0±0.8	0.0036
	Fe-Fe	6	2.86±0.01	0.0060		
FeN_4-CMPCFs	Fe-N	4.0±0.2	1.98±0.01	0.0084	-4.4±1.3	0.0067
Fe_2N_6-CMPCFs	**Fe-N1**	2.1±0.2	**1.89±0.01**	0.0033	-2.5±1.5	0.0053
	Fe-N2	1.9±0.4	**2.01±0.01**	0.0033		
	Fe-Fe	1.0±0.1	2.55±0.01	0.0121		

${}^{a}N$: coordination numbers; ${}^{b}R$: bond distance; ${}^{c}\sigma^2$: Debye-Waller factors; ${}^{d}\ \Delta E_0$: the inner potential correction. *R* factor: goodness of fit.

Note: The obtained XAFS data was processed in Athena (version 0.9.26) for background, pre-edge line and post-edge line calibrations. Then Fourier transformed fitting was carried out in Artemis (version 0.9.26). The k^3 weighting, k-range of 3~13 $Å^{-1}$ and R range of 1~3 Å were used for the fitting of Fe foil; k-range of 3~12 $Å^{-1}$ and R range of 1~2.5 Å were used for the fitting of FeN_4-CMPCFs, Fe_2N_6-CMPCFs. The four parameters, coordination number, bond length, Debye-Waller factor and E_0 shift (CN, R, ΔE_0) were fitted without anyone was fixed, the σ^2 was set.

Table S5. The adsorption free energy (eV) ΔG_{OOH*}(or $\Delta G_{OH\text{-}O*}$), ΔG_{O*}(or $\Delta G_{OH\text{-}O*}$) and ΔG_{OH*} of each model

	ΔG_{OOH*} or $\Delta G_{OH\text{-}O*}$	ΔG_{O*} or $\Delta G_{OH\text{-}OH*}$	ΔG_{OH*}
FeN_4	3.634	1.675	0.801
FeN_4-C_h	3.749	1.785	0.948
FeN_4-C_h-N_{py}	3.858	1.994	1.094
Fe_2N_6OH	3.348	1.993	0.902
Fe_2N_6OH-C_h	3.681	2.370	1.031
Fe_2N_6OH-C_h-N_{py}	3.929	2.476	1.177

Table S6. The reaction free energy (eV vs RHE) of elementary step for ORR (ΔG_1, ΔG_2, ΔG_3, ΔG_4) at U_{RHE}=0V and potential determining step for ORR (red)

	ΔG1	ΔG2	ΔG3	ΔG4
FeN_4	-1.282	-1.958	-0.875	-0.801
FeN_4-C_h	-1.167	-1.964	-0.837	-0.948
FeN_4-C_h-N_{py}	-1.058	-1.864	-0.900	-1.094
Fe_2N_6OH	-1.568	-1.355	-1.090	-0.902
Fe_2N_6OH-C_h	-1.235	-1.311	-1.339	-1.031
Fe_2N_6OH-C_h-N_{py}	-1.037	-1.395	-1.305	-1.179

Table S7. Theoretical overpotential for ORR (U^{over}, V vs RHE) of each model.

	$U^{over}{}_{ORR}$
FeN_4	0.428
FeN_4-C_h	0.392
FeN_4-C_h-N_{py}	0.329
Fe_2N_6OH	0.327
Fe_2N_6OH-C_h	0.198
Fe_2N_6OH-C_h-N_{py}	0.192

Table S8. The d-band centers (eV vs. Fermi Energy) of Fe atoms in various models

	Spin-up	**Spin-down**	**Type**
FeN_4	-2.393	0.616	Fe(II)
FeN_4-C_h	-2.300	0.692	Fe(II)
FeN_4-C_h-N_{py}	**-2.199**	**0.791**	Fe(II)
Fe_2N_6OH-C_h-N_{py}	-3.768	0.100	Fe(II)&Fe(III)
Fe_2N_6OH-C_h-N_{py}	**-3.643**	**0.018**	Fe(II)
Fe_2N_6OH-C_h-N_{py}	-3.894	0.182	Fe(III)

Table S9. The –ICOHP (eV) of Fe-N bonds in various models.

	Fe-N1	**Fe-N2**	**Fe-N3**	**Fe-N4**	**Total Fe-N**
FeN_4	2.299	2.340	2.301	2.341	**9.280**
FeN_4-C_h	2.345	2.432	2.360	2.457	**9.594**
FeN_4-C_h-N_{py}	2.357	2.392	2.379	2.439	**9.567**
Fe_2N_6OH-C_h-N_{py}	2.211	2.305	3.073	3.157	**10.747**

Table S10. Contributions of various orbitals of Fe to the –ICOHP (eV) of Fe(orbital)-N in various models.

	4s	**$3dx^2$-y^2**	**$3dz^2$**	**3dxy**	**3dxz**	**3dyz**
FeN_4	3.670	3.000	0.618	1.129	0.410	0.453
FeN_4-C_h	3.642	3.110	0.650	1.223	0.455	0.516
FeN_4-C_h-N_{py}	3.650	3.121	0.643	1.207	0.439	0.508
Fe_2N_6OH-C_h-N_{py}	3.925	3.382	0.740	1.638	0.606	0.455

Note: The 4s, $3dx^2$-y^2, $3dz^2$ and 3dxy orbital interaction are regarded as σ interaction of Fe-N.

Table S11. Contributions of typical orbital interactions in Fe-Fe bond in Fe_2N_6OH-C_h-N_{py} system to the -ICOHP (eV).

	Fe_2N_6OH-C_h-N_{py}
4s - 4s	**0.197**
$3dx^2$-y^2 - $3dx^2$-y^2	0.005
$3dz^2$ - $3dz^2$	0.000
3dxy – 3dxy	**0.092**
3dxz – 3dxz	-0.002
3dyz – 3dyz	0.006

Table S12. The partial charges of Fe(II) and coordinated N atoms in various models.

	N1	**N2**	**N3**	**N4**	**Fe**	**Type**
FeN_4	-0.65	-0.65	-0.65	-0.65	1.30	Mulliken
FeN_4-C_h	-0.64	-0.65	-0.63	-0.63	1.31	Mulliken
FeN_4-C_h-N_{py}	**-0.63**	**-0.65**	**-0.62**	**-0.62**	**1.31**	Mulliken
Fe_2N_6OH-C_h-N_{py}	**-0.61**	**-0.64**	**-0.83**	**-0.86**	**1.45**	Mulliken
FeN_4	-0.44	-0.44	-0.44	-0.44	1.06	Loewdin
FeN_4-C_h	-0.44	-0.45	-0.41	-0.43	1.07	Loewdin
FeN_4-C_h-N_{py}	**-0.44**	**-0.44**	**-0.41**	**-0.42**	**1.07**	Loewdin
Fe_2N_6OH-C_h-N_{py}	**-0.43**	**-0.44**	**-0.66**	**-0.70**	**1.23**	Loewdin

Table S13. Comparison of liquid-state ZABs.

Catalyst	Open circuit voltage [V]	Peak power density [mW cm^{-2}]	Cycling current density [mA cm^{-2}]	Cycling stability	Ref.
This work	**1.57**	**261.4**	**5**	**14, 500 cycles (4800 h)**	
PdMo bimetallene/C	1.48	154.2	10	350 cycles (500 h)	*Nature* **2019**, 574, 81.
Ni-NHGF	/	158	2	90 cycles (30 h)	*Nat. Catal.* **2018**, 1, 63
HESA	1.48	207	2	50 cycles (200 h)	*Nat. Sustain.* **2023,** 6, 816–826
CoNC SAC	/	161.8	5	480 cycles (80 h)	*Sci. Adv.* 8, eabn5091(**2022**)
Co SA-NDGs	1.53	251.4	5	350 cycles (350 h)	*Nat. Commun.* 13, 3689 (**2022**)
Fe,Mn/N–C catalyst	1.4	160.8	5	735 cycles (81 h)	*Nat. Commun.* 12, 1734 (**2021**)
(Co,Fe)$_3$N-2D	/	234	5	38 cycles (750 h)	*Nat. Commun.* **2020**, 11, 1952
hybrid ZAB	1.50	/	0.5	2600 h	*Joule* 6 (**2022**),1617-1631
Fe$_H$–N–C	1.53	225	5	1800 cycles (1200 h)	*Adv. Mater.* **2023**, 35, 2210714
Alk-MXene/FePc	1.49	191.5	/	/	*Adv. Mater.* **2023***,* 35, 2210757
Fe/SNCFs-NH$_3$	1.38	255.84	1	1000 cycles (1000 h)	*Adv. Mater.* **2022**, 34, 2105410
Fe/Meso-NC-1000	1.52	109.6	5	40 h	*Adv.Mater.* **2022**, 34, 2107291
Fe$_{0.5}$Co@HOMNCP	1.62	134	2	120 h	*Adv.Mater.* **2022**, 34, 2109605
P/Fe−N−C	1.48	269	10	576 cycles (192 h)	*J. Am. Chem. Soc.* **2023**, 145, 3647−3655
Co$_2$P/CoN$_4$@NSC-500	1.45	134.5	5	3485 cycles (1742 h)	*Angew. Chem.Int. Ed.* **2023**,62,e202216950
hydrophobic-Co$_3$O$_4$ NSs/CC	1.42	171	5	500 cycles (166 h)	*Angew. Chem. Int. Ed.* **2022**, 61, e202202671
Fe-N-GDY	/	249	2	900 cycles	*Angew. Chem. Int. Ed. **2022**, 61, e202208238*
Fe-N,O/G	1.55	164.7	/	/	*Energy Environ. Sci.*, **2023**, https://doi.org/10.1039/D3EE00747B

Table S14. Comparison of flexible solid-state ZABs.

Catalyst	Peak power density [mW cm^{-2}]	Cycling current density [mA cm^{-2}]	Cycling stability	Ref.
This work	**203.7**	**2**	**160 h**	
Fe/SNCFs-NH$_3$	/	1	60 h	*Adv. Mater.* **2022**, 34, 2105410
MoS$_2$/Fe-N-C	78	5	17 h	*Proc. Natl. Acad. Sci. U.S.A.* **2021,** 118, e2110036118
CoS/Fe$_3$S$_4$@SNCP	117	10	30 h	*Adv. Energy Mater.* **2023**, 13, 2204245
CoCNTs/PNAs	/	2	43 h	*Adv. Energy Mater.* **2023**, 13, 2202871
IE-NiCoFe/HPLIG	88	5	84 h	*Adv. Energy Mater.* **2022**, 12, 2200906
MXene/Zn-LDH-array@PVA	92.3	3	50 h	*Adv. Energy Mater.* **2022**, 12, 2201393
FeMn-DSAC	184	2	80 h	*Angew. Chem. Int. Ed.* **2022**, 61, e202115219
Fe,Co,N-C	158	2	34 h	*ACS Nano* **2022**, 16, 7890−7903
Ni-SAs/HCNFs/Co-NAs	57.6	10	82 h	*ACS Nano* **2022**, 16, 9, 15273−15285
Fe$_1$/d-CN	78	1	20 h	*Energy Environ. Sci.* **2021**, 14, 6455–6463
Fe SA/NCZ	101	2	44 h	*Adv. Funct. Mater.* **2023**, 33, 2213897
IW-Co$_3$O$_4$-RuO$_2$-HS	64.5	/	30 h	*Adv. Funct. Mater.* **2022**, 32, 2203206

4. Reference

1. Q. Luo, K. Wang, Q. Zhang, W. Ding, R. Wang, L. Li, S. Peng, D. Ji and X. Qin, *Angewandte Chemie International Edition*, **n/a**, e202413369.
2. G. Kresse and J. Furthmüller, *Comput. Mater. Sci.*, 1996, **6**, 15-50.
3. G. Kresse and J. Furthmüller, *Phys. Rev. B*, 1996, **54**, 11169-11186.
4. J. P. Perdew, K. Burke and M. Ernzerhof, *Phys. Rev. Lett.*, 1996, **77**, 3865-3868.
5. G. Kresse and D. Joubert, *Phys. Rev. B*, 1999, **59**, 1758-1775.
6. K. Mathew, R. Sundararaman, K. Letchworth-Weaver, T. A. Arias and R. G. Hennig, *J. Chem. Phys.*, 2014, **140**.
7. V. I. Anisimov, J. Zaanen and O. K. Andersen, *Phys. Rev. B*, 1991, **44**, 943-954.
8. H. Xu, D. Cheng, D. Cao and X. C. Zeng, *Nat. Catal.*, 2018, **1**, 339-348.
9. J. K. Nørskov, J. Rossmeisl, A. Logadottir, L. Lindqvist, J. R. Kitchin, T. Bligaard and H. Jónsson, *J. Phys. Chem. B*, 2004, **108**, 17886-17892.
10. W. Zou, R. Lu, X. Liu, G. Xiao, X. Liao, Z. Wang and Y. Zhao, *J. Mater. Chem. A*, 2022, **10**, 9150-9160.
11. V. Wang, N. Xu, J.-C. Liu, G. Tang and W.-T. Geng, *Compu. Phys. Commun.*, 2021, **267**, 108033.
12. R. Dronskowski and P. E. Blöchl, *J. Phys. Chem. C*, 1993, **97**, 8617-8624.
13. V. L. Deringer, A. L. Tchougréeff and R. Dronskowski, *J. Phys. Chem. A*, 2011, **115**, 5461-5466.
14. S. Maintz, V. L. Deringer, A. L. Tchougréeff and R. Dronskowski, *J. Comput. Chem.*, 2013, **34**, 2557-2567.
15. R. Nelson, C. Ertural, J. George, V. L. Deringer, G. Hautier and R. Dronskowski, *J. Comput. Chem.*, 2020, **41**, 1931-1940.